Journal of Applied Physics

# Synthesis, properties, and applications of 2D amorphous inorganic materials

Cite as: J. Appl. Phys. **127**, 220901 (2020); https://doi.org/10.1063/1.5144626
Submitted: 09 January 2020 • Accepted: 23 May 2020 • Published Online: 08 June 2020

Zhibin Yang, Jianhua Hao and Shu Ping Lau



Journal of Applied Physics PERSPECTIVE scitation.org/journal/jap

# Synthesis, properties, and applications of 2D amorphous inorganic materials

Cite as: J. Appl. Phys. **127**, 220901 (2020); doi: 10.1063/1.5144626
Submitted: 9 January 2020 · Accepted: 23 May 2020 ·
Published Online: 8 June 2020

View Online Export Citation CrossMark

Zhibin Yang,[1,2] Jianhua Hao,[2,3,a)] and Shu Ping Lau[2,a)]

## AFFILIATIONS

[1]Center for Terahertz Waves and College of Precision Instruments and Optoelectronics Engineering, Tianjin University, No. 92 Weijin Road, Tianjin 300072, People's Republic of China
[2]Department of Applied Physics, The Hong Kong Polytechnic University, Hung Hom, Hong Kong 999077, People's Republic of China
[3]The Hong Kong Polytechnic University Shenzhen Research Institute, Shenzhen 518057, People's Republic of China

[a)]**Authors to whom correspondence should be addressed:** jh.hao@polyu.edu.hk and apsplau@polyu.edu.hk

## ABSTRACT

In the last decade, the research on two-dimensional (2D) materials has drawn a lot of interest from the aspects of both fundamental study and practical application. The atomic-scale thickness and unique layered structure make the materials in this family exhibit a number of distinct optical and electrical properties from their bulk counterparts. Previous studies have mainly focused on the crystalline 2D candidates. Recently, the highly disordered form of 2D materials, such as amorphous 2D materials, is emerging to attract increasing attention since it has shown great potential for applications in various fields. Here, we give a perspective on the recent progress in 2D amorphous inorganic materials. First, the synthesis techniques and process of 2D amorphous materials and their hybrid structure are given. Furthermore, the intriguing properties and applications in electronic, optoelectronic, and energy fields from typical 2D amorphous inorganic materials, including amorphous graphene, amorphous molybdenum disulfide, amorphous boron nitride, and amorphous black phosphorus, are introduced. Furthermore, the advantages and mechanisms of 2D amorphous materials are illustrated, pointing out the application scope of this material group. Finally, the underlying challenges of amorphous inorganic 2D materials are briefly outlined and some future outlooks are suggested.



## I. INTRODUCTION

The rise of two-dimensional (2D) layered materials opens a new era to a new variety of possibilities for materials science and nanotechnology.[1–3] Thanks to the layered structure and atomic-scale thickness, 2D materials not only preserve features of the bulks but also exhibit their own distinctive peculiarities, showing great potential for next-generation electronics, optoelectronics, energy applications, and so on.[4–6] As the first and most studied 2D member, graphene has attracted great research interest since it was isolated from graphite crystal.[7] The remarkable electron mobility, high optical transparency, and considerable thermal conductivity make it promising for high-speed electronic devices.[8] Besides graphene, numerous 2D layered semiconductors have been discovered in recent years, such as transition metal dichalcogenides (TMDs),[9–11] ultrathin black phosphorus (BP),[12,13] and 2D III-VI semiconductors,[14,15] which could ideally make up for the lack of a bandgap in graphene. Compared to conventional semiconductors, 2D semiconductors usually have layer-dependent electronic bandgaps and favorable flexibility, which are propitious for wearable and broadband photonic and optoelectronic devices.[16–20] Very recently, superconductivity,[21] ferroelectricity,[22,23] and ferromagnetism[24] have been observed in 2D materials as well. Moreover, 2D materials can form van der Waals (vdW) heterostructures simply by assembling different 2D layers in the vertical or lateral way, realizing some new attractive characteristics, which largely extend the application horizon of this family.[25,26]

Until now, the research on 2D materials mainly focuses on the crystalline counterpart, while the study of highly disordered form is much less. Compared to a crystalline system, amorphous materials are short of long-range and predictable atomic order, resulting in very complicated electronic states, which severely limit the performance of electronic devices.[27] Nevertheless, the unique non-

crystalline structure, excellent large-area uniformity, and low fabrication cost make them play important roles in various industrial applications.[28,29] In general, it is well-known that the electronic structures of amorphous materials are controlled by their defects and impurities.[30] However, it has been reported that the strong ionicity of amorphous oxide semiconductors could lead to carrier transport properties comparable to those of crystalline materials since strong ionic bonds are not altered largely by the highly disordered structure, making them suitable for high-performance thin film transistor (TFT) applications.[28,31] Moreover, the luxuriant defects within amorphous materials provide abundant active sites, which endow them promising for catalysis applications.[32,33] Besides, amorphous silicon dioxide (a-$SiO_2$) has been the most commonly used gate insulating layer in logic electronic devices owing to its considerable and uniform dielectric property.[34,35] In addition, Toh *et al.* have synthesized a large-area, free-standing monolayer amorphous carbon by laser-assisted chemical vapor deposition (CVD) method, which exhibits attractive insulating properties with high stability, proving that the material is applicable for magnetic recording applications.[36] Recently, the highly disordered form of 2D materials, namely, amorphous 2D materials, have been studied since new fascinating features are generated by the combination of a 2D system and an amorphous structure.[37–40] In general, amorphous 2D materials have a similar configuration as their crystalline counterpart, which exhibit continuous 2D arrangements of atoms and a layered structure but with abundant defects and randomly distributed stacks without any specific orientation. So far, a variety of amorphous 2D materials have been synthesized, including amorphous graphene (a-graphene),[41,42] amorphous TMDs (a-TMDs),[37,43,44] amorphous BP (a-BP),[38] and amorphous boron nitride (a-BN),[45,46] which demonstrate distinct properties to crystalline ones and applications in electronics, optoelectronics, energy storage, and electrocatalyst fields (Fig. 1).

Up to now, many research studies have been published on the study of 2D materials.[2,3,10,26] Among them, there are a few review articles introducing 2D amorphous nanomaterials,[27,40,47] which mainly concentrate on ultrathin amorphous materials, such as 2D oxides, organic materials, and so on. To the best of our knowledge, there is currently no perspective article specifically on the non-crystalline form of 2D inorganic materials, such as a-graphene, a-BP, and a-$MoS_2$. Compared with organic materials, most of the inorganic materials exhibit a predictable band structure and controllable features, which benefit for developing electronic, optoelectronic, and energy applications. Considering the number of publications on amorphous inorganic 2D materials is growing in recent years, it is essential to provide an overview and perspective on the research in this area. Hence, the recent efforts and progress of amorphous inorganic 2D materials are systematically discussed in this perspective article. Initially, the synthesis techniques for different types of 2D amorphous inorganic materials will be briefly introduced with the merits and growth mechanisms. Then, the distinctive properties as well as representative applications of these 2D amorphous materials are analyzed and demonstrated, respectively. At last, the article is summarized with our perspectives. The latent challenges and potential outlook in the field are also provided.

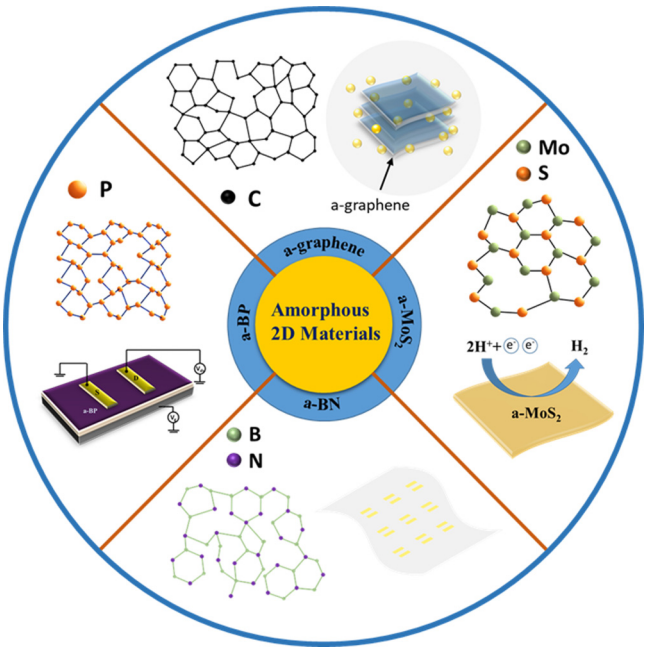


**FIG. 1.** Diverse amorphous 2D inorganic materials (a-graphene, a-$MoS_2$, a-BN, and a-BP) and various applications of these materials (transformer oil nanofluids, hydrogen evolution reaction, flexible electronic device, field-effect transistors, respectively).

## II. SYNTHESIS TECHNIQUES OF 2D AMORPHOUS MATERIALS

So far, the natural bulk of amorphous inorganic 2D materials has not been found yet, and layered stacks are randomly distributed, which is not suitable for exfoliation, implying that the only way to obtain ultrathin amorphous 2D films is either directly growing by bottom–up techniques or phase transformation from crystalline form. Initially, Kotakoski *et al.* found that the electron irradiation could effectively adjust the bond rotation and atom ejection in graphene, which transformed graphene into an amorphous membrane with random distribution of polygons.[48] However, the obtained sample usually possesses small size and the quality is hard to be controlled. In comparison, the vapor phase based bottom–up methods, mainly including CVD and physical vapor deposition (PVD), are commonly used for scalable synthesis of 2D materials.[49–51] Recently, these two types of techniques are also considered applicable for successfully growing 2D amorphous thin films.[27] In this section, we introduce the features and mechanisms of growing 2D amorphous materials by CVD and PVD, respectively.

### A. CVD growth of amorphous 2D materials

Since CVD is considered as the most competent approach for fabricating a wafer-scale graphene film, the technique has already been extended for the preparation of other 2D materials and heterostructures in recent years.[52–54] By precisely manipulating the

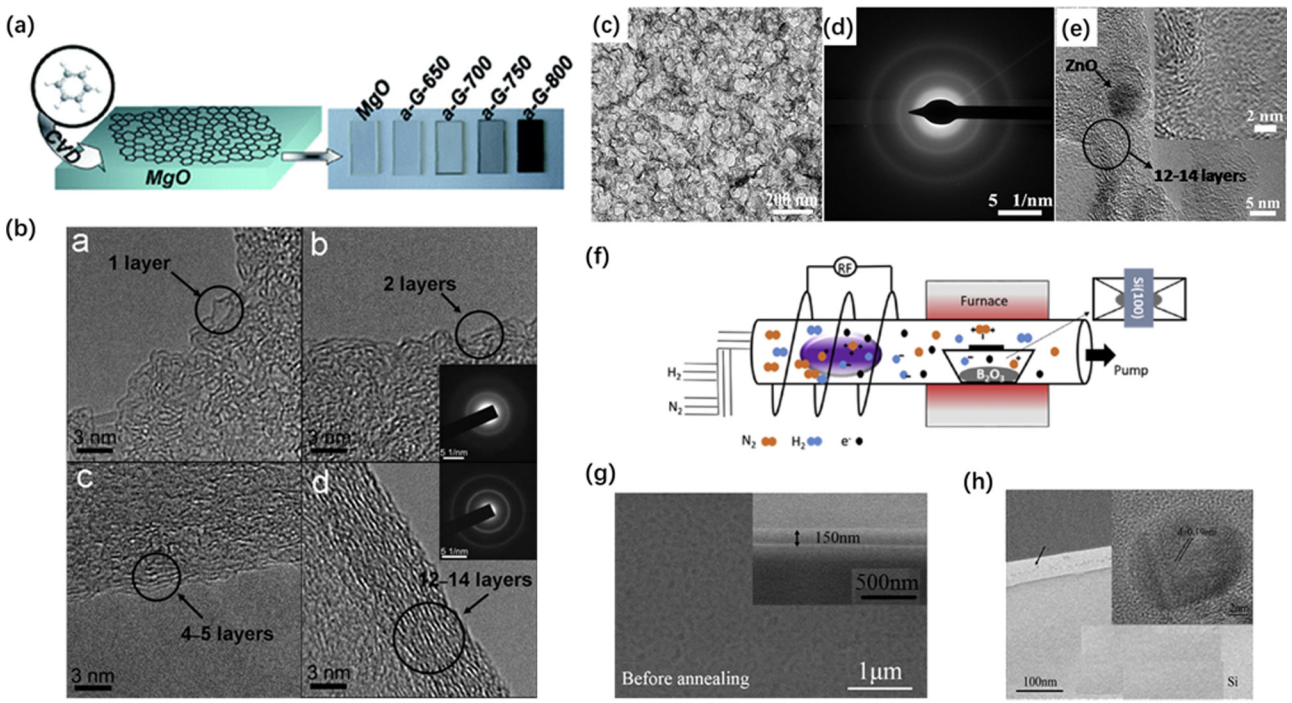


**FIG. 2.** Amorphous 2D materials synthesized by the CVD method. (a) The schematic and optical pictures of an a-graphene film grown on MgO substrates under different temperatures by CVD. (b) Cross-sectional TEM images of a-graphene films prepared under different temperatures. The inset images show the SAED results of films grown under 700 °C and 800 °C, respectively. Reproduced with permission from Zhao *et al.*, J. Mater. Chem. **22**, 19679 (2012). Copyright 2012 The Royal Society of Chemistry. (c) and (d) The TEM image of the SAED pattern of an a-graphene film grown on the ZnO/Si substrate, respectively, demonstrating the morphology and amorphous phase of the films. (e) The high-resolution TEM image of the edge of a-graphene film. The inset shows the enlarged TEM image. Reproduced with permission from Li *et al.*, Synth. Met. **174**, 50 (2013). Copyright 2013 Elsevier. (f) The schematic of a-BN film grown by PECVD system. (g) SEM image of the obtained a-BN film before annealing process. The inset shows the cross-sectional SEM image of a-BN/Si. (h) The TEM image of an a-BN film. The inset shows the nanograins decorated on the amorphous film. Reproduced with permission from Li *et al.*, J. Alloys Compd. **705**, 734 (2017). Copyright 2017 Elsevier.

precursors, substrates, pressure, and temperature during the deposition process, the grain size, morphology, defects, dopants, and layer number of the CVD products can be appropriately controlled to fit the requirement with high reproducibility,[36,55] which may also give rise to the highly disordered phase of the materials. Compared to the growth of crystalline 2D materials, the synthesis process of amorphous counterparts is rather complicated since the non-crystalline state is unstable with the tendency to transform into crystalline phase.[27] Thus, suppressing such transformation by controlling the synthesis process is significant for growing 2D amorphous materials.

Previous studies have shown that adding oxygen or hydrogen during CVD growth of graphene could help one to promote the graphitization and eliminate the proportion of amorphous states.[56,57] In the opposite way, the non-crystalline phase could be increased by making use of the oxygen-free CVD with hydrogen deficient precursors. Based on this strategy, Huang *et al.* have successfully synthesized large-scale undoped and n-doped a-graphene (N-a-graphene) films on MgO (100) substrates by CVD, where benzene and pyridine were used as precursors, respectively.[58] In this study, the quality of a-graphene grown under different processing temperature was characterized. According to the optical images of a-graphene [Fig. 2(a)], the transparency of the films decreases gradually when raising the growth temperature from 650 °C to 800 °C since higher temperature tends to form thicker films. The result also illustrates that the a-graphene film fully covers the substrates with high continuity. Further structural characterization, including transmission electron microscopy (TEM), x-ray photoelectron spectroscopy (XPS), and Raman spectroscopy, verified that the obtained films possess non-crystalline phase of graphene. Remarkably, the a-graphene films may preserve the layered structure as well [Fig. 2(b)], which is one of the typical signs of 2D materials. Meanwhile, the layer number and the crystallinity of a-graphene films are strongly dependent on the growth temperature, implying that the properties of a-graphene can be tuned by the fabrication conditions.

Besides temperature, substrates also play a significant role in the quality of CVD grown films.[59,60] With almost identical synthesis conditions of the previous work, a honeycomb-like a-graphene film was realized on the buffer layer of zinc oxide (ZnO) film by CVD.[61] As shown in Fig. 2(c), numerous bowl-like graphene walls are formed within the film, which exhibit the amorphous phase according to the selected area electron diffraction (SAED) pattern

[Fig. 2(d)]. The sizes of holes encircled by graphene walls are around 10–100 nm, which are close to the sizes of ZnO grains. Moreover, the cross-sectional TEM image shows that the thickness of the a-graphene film is around 5 layers while the graphene walls are composed of 12–14 layers, which are exactly supported by the ZnO nanocrystals [Fig. 2(e)]. This work evidences that the oxide films could enable the formation of a-graphene films and govern their topology during CVD process. Furthermore, as ZnO is a powerful semiconductor for applications of optoelectronics and energy harvesting devices,[62] the hybrid structure of a-graphene and ZnO film would have broader application prospects.

The standard CVD method suffers from relatively a high growth temperature, which largely limits its usage in fabricating flexible transparent devices.[55] To overcome this limitation, a plasma-enhanced CVD (PECVD) system has been designed, which could effectively lower the processing temperature by utilizing an inert gas plasma.[63,64] Meanwhile, the controllability of nanostructure formation and uniformity of the films are highly enhanced for PECVD fabrication thanks to the existence of plentiful excited carriers in the plasma. In a recent study, a mixed amorphous form of a boron nitride (BN) thin film with excellent field emission (FE) performance was synthesized by the PECVD method.[65] As shown in Fig. 2(f), a radio frequency was applied to create the plasma by ionizing the flowing $N_2$ and $H_2$ gases, which further nitridizes the $B_2O_3$ powder in the center of the furnace. According to the scanning electron microscopy (SEM) image [Fig. 2(g)], the obtained film has a relatively uniform surface and the thickness is around 150 nm. Furthermore, the TEM image exhibits that the main area of the film is non-crystalline but with some nanocrystalline grains [Fig. 2(h)], indicating that the obtained BN film has a mixed amorphous structure. Compared to previous works, PECVD is a nontoxic and low cost technique for large-area synthesis of an a-BN film.[65]

Besides PECVD, atomic layer deposition (ALD) is also a powerful CVD method for thin film deposition under a low processing temperature, which is ideal for producing uniform, large-area films with good thickness controllability.[66] Recently, Shin *et al.* reported that an a-$MoS_2$ film was realized on an Si wafer capped with a thin layer of Au by ALD.[67] The fabrication was carried out at a low temperature of 100 °C with molybdenum hexacarbonyl [$Mo(CO)_6$] and dimethyl disulfide ($CH_3S_2CH_3$) as precursors. The obtained a-$MoS_2$ demonstrates excellent electrochemical performance thanks to the high-disordered structure. Furthermore, Song *et al.* have utilized a pressure-tuned stop-flow ALD technique for depositing a-$MoS_2$ thin films on carbon nanotube (CNT) substrates at 80 °C with the same precursors.[68] A uniform non-crystalline $MoS_2$ film with the thickness of 5 nm was obtained, and the surface was partially oxidized because of the highly chemical activity, which is propitious to the oxygen evolution reaction (OER) as cathode materials. Up to now, only a-$MoS_2$ was reported to be realized by ALD. Considering its advantages for synthesizing highly uniform thin films at low temperature, more materials and investigation should be carried out in the future.

### B. PVD growth of amorphous 2D materials

PVD is another alternative method for scalable growth of 2D materials.[69] In general, the fabrication of PVD is carried out in a high vacuum circumstance, inside which the target materials with condensed state are transformed to vapor phase and then converted to thin film state by a variety of physical means.[70,71] The commonly used PVD techniques include pulsed laser deposition (PLD), sputtering deposition, thermal evaporation, and cathodic arc deposition. Compared to CVD, PVD methods usually have higher growth rate and better control of film thickness.[70] Moreover, PVD is applicable for those materials with high chemical sensitivity, making it an indispensable complement method to CVD.

Among various PVD techniques, PLD is widely known for its features like pulsed deposition mode and stoichiometric transfer of target composition,[70] which makes it widely used for growing complex oxide thin films,[72–74] superlattices,[75,76] and heterostructures.[77–79] In recent studies, PLD has begun to be used in the synthesis of 2D materials, including both crystalline and amorphous phases.[51,80–83] In principle, an energetic pulsed laser is utilized during fabrication process of PLD. The target material can be ablated out by the focused laser beams and then form thin films on the substrate [Fig. 3(a)]. However, the energy is insufficient to promote the crystallization of the film at a relatively low temperature, which offers the possibility to synthesize amorphous 2D materials by PLD.[27] In a recent study, ultrathin a-BN films with the thickness ranging from 2 to 17 nm were successfully prepared by PLD [Fig. 3(a)].[46] As shown in the optical images, the obtained films could fully cover the substrates with an area as large as 3 in., which is much larger than those of crystalline BN films.[84] Meanwhile, the continuous and uniform thickness was confirmed by the cross-sectional TEM. Thanks to the versatility in materials processing of PLD, a-BN films can be realized on various substrates at a low processing temperature (<200 °C), including metals (e.g., copper foil, nickel foil, etc.), ceramics (e.g., $SiO_2$/Si, $Al_2O_3$, etc.), flexible polymers (e.g., Kapton, PDMS, etc.), and other 2D materials (e.g., graphene, few-layer $MoS_2$, etc.), making them applicable for diverse applications.

Among the family of 2D materials, phosphorene has great potential for novel applications in electronics due to its tunable bandgaps and exceptionally high carrier mobility.[85,86] However, 2D BP suffers from its high instability, which largely limits its wafer-scale synthesis.[87,88] Recently, our team has first demonstrated the PLD method to prepare centimeter-scale BP ultrathin films with a highly disordered structure, which was named as a-BP [Fig. 3(b)].[38] Compared with crystalline BP, the lattice of a-BP exhibits a short-range order with altering bonding angle and length. The growth temperature window of a-BP is very narrow according to the Raman spectra of films prepared under different temperatures, where the BP characteristic peaks can only be observed at around 150 °C [Fig. 3(c)]. Moreover, the amorphous nature of the films is confirmed by both high-resolution TEM (HRTEM) and SAED pattern [Fig. 3(d)]. The obtained a-BP films not only preserve the thickness-tunable optical bandgaps but also demonstrate promising electronic performance. The details of properties and device characterization of an a-BP film will be discussed in the Sec. III.

A previous study shows that PLD is suitable for depositing large-area $MoS_2$ films without adding any catalysts.[89] In PLD processes, only the stoichiometric ratio is replicated from the target, and the crystallization could be changed, depending on the fabrication conditions, which provides the possibility to grow amorphous

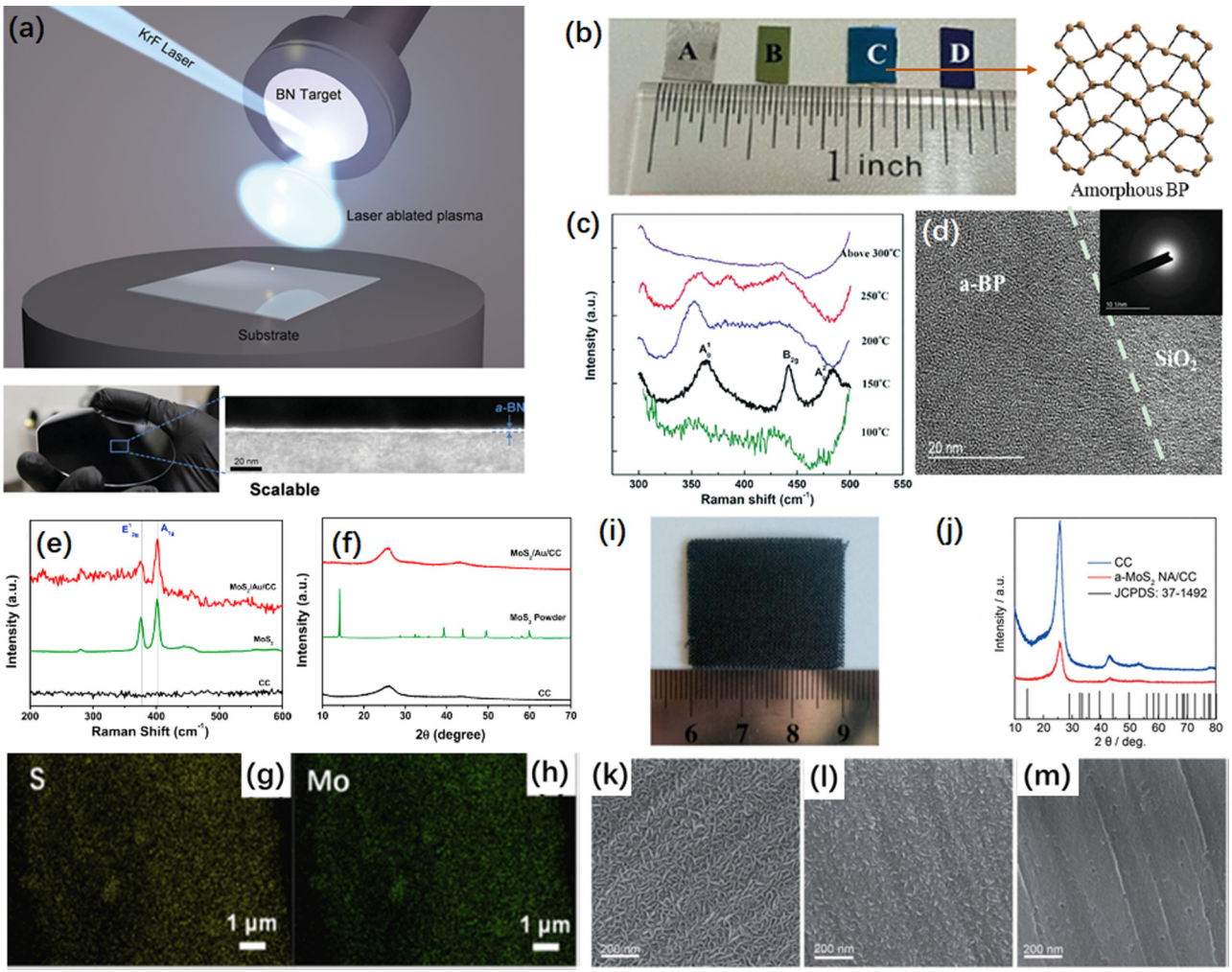


**FIG. 3.** PVD method grown amorphous 2D materials. (a) Up: Schematic picture of fabrication process of an a-BN film by PLD. Below: Optical picture of an a-BN film on an Si wafer and a cross-sectional TEM image of a-BN/$Al_2O_3$. Reproduced with permission from Glavin *et al.*, Adv. Funct. Mater. **26**, 2640 (2016). Copyright 2016 Wiley-VCH. (b) Left: Optical pictures of a-BP films grown under different substrates and temperatures. Right: Schematic of the atomic structure of an a-BP film. (c) Raman spectra of a-BP films grown under different substrate temperatures. (d) HRTEM image of an a-BP film. The inset shows the SAED pattern, revealing the amorphous nature of the film. Reproduced with permission from Yang *et al.*, Adv. Mater. **27**, 3748 (2015). Copyright 2015 Wiley-VCH. (e) and (f) Raman spectra and XRD results of a-$MoS_2$/Au/CC, barely crystalline $MoS_2$ and CC substrates, respectively. (g) and (h) EDX mapping of both S and Mo for an a-$MoS_2$ thin film. Reproduced with permission from Wang *et al.*, Electrochim. Acta **258**, 876 (2017). Copyright 2017 Elsevier. (i) Photograph of an a-$MoS_2$ film grown on a CC substrate. (j) XRD patterns of CC, a-$MoS_2$/CC, and standard JCPDS pattern of crystalline $MoS_2$. (k)–(m) SEM images of a-$MoS_2$ films grown under different sputtering powers with (k) 100 W, (l) 70 W, and (m) 150 W. Reproduced with permission from Zhang *et al.*, J. Mater. Chem. A **3**, 19277 (2015). Copyright 2015 The Royal Society of Chemistry.

2D materials. Recently, a-$MoS_2$ thin films were prepared on gold-coated carbon cloth (Au/CC) substrates by PLD at room temperature (RT).[89] The Raman spectrum and x-ray diffraction (XRD) pattern confirms that the obtained films are $MoS_2$ with a non-crystalline structure [Figs. 3(e) and 3(f)]. Compared to the commercial $MoS_2$, the a-$MoS_2$ film shows a particle-like structure with a rough surface, which could optimize the electrochemical performance by providing a larger reaction surface. The energy-dispersive x-ray spectroscopy (EDX) result confirms that element ratio of Mo and S is around 1:2, and the mapping images show the homogeneous growth of the film [Figs. 3(g) and 3(h)]. The large-area and unique surface structure of PLD grown a-$MoS_2$ could provide more active sites for HER catalytic activity.

Apart from PLD, sputtering is a commonly used PVD method for synthesizing amorphous 2D materials.[37,90,91] A recent work done by Wan's group has shown the capability of successfully growing large-area a-$MoS_2$ nanosheet arrays on the CC substrate by a reproducible magnetron sputtering system [Fig. 3(i)].[90] The amorphous

**TABLE I.** Summary of synthesis techniques of amorphous 2D materials.

| Materials | Synthesis methods | Processing temperature (°C) | Size of products | Reference |
|---|---|---|---|---|
| a-graphene | CVD | 650–800 | 10 × 5 × 0.5 mm | 58 |
| | CVD | 700–800 | Wafer-scale | 61 |
| | Ultrasonication | ~250 | 500–600 nm | 39 |
| a-$MoS_2$ | PLD | RT | 0.5 $cm^2$ | 92 |
| | Sputtering | … | 30 × 30 mm | 90 |
| | ALD | 150 | ~20 nm | 68 |
| | Hydrothermal reaction | 90–120 | ~30 nm | 93 |
| a-BN | PECVD | 1000 | >5 $\mu$m | 65 |
| | PLD | <200 | 3 in. | 46 |
| | Sputtering | RT | … | 91 |
| a-BP | PLD | ~150 | Centimeter scale | 38 |

nature is verified by XRD results [Fig. 3(j)]. By altering the sputtering power, the morphology of the a-$MoS_2$ film can be dramatically modified according to the SEM images [Figs. 3(k)–3(m)]. With sputtering power increasing from 70 W to 150 W, the film morphology changes from small nanofibers to densely compacted nanosheet arrays, and then eventually achieving a smooth uniform film. The variation of the morphology makes the HER performance of a-$MoS_2$ films tunable by fabrication conditions of sputtering.

In addition to the techniques discussed above, there are some other methods that can be utilized for growing amorphous 2D materials.[93–96] As summarized in Table I, most of the films grown by CVD or PVD methods have a large size and relatively low processing temperature, paving the way to realize uniform devices over wafer-scale substrates. According to the above discussion, typical bottom–up techniques are efficient for preparing ultrathin amorphous 2D films, which can build the basis for the development of applications.

## III. PROPERTIES AND APPLICATIONS OF AMORPHOUS 2D MATERIALS

Thanks to the short-range atomic arrangement, amorphous materials possess some distinct characteristics, such as a large number of defects,[97] exceptional transport path of carriers,[98] and ultra-uniform surface,[99] which greatly promote their device performance in energy storage,[100] electrocatalysis,[32] and electronics fields.[99] Benefiting from the above features as well as the ultrathin structure, 2D amorphous materials have their own particularities and applicable scope. For instance, the large in-plane size could enhance the generation of defects by providing a larger specific surface, which benefits for the function as catalyst.[92] In this section, the unique properties and applications of typical amorphous 2D materials, including a-graphene, a-$MoS_2$, a-BN, and a-BP will be illustrated in sequence. The performance and mechanism of the devices will also be discussed.

### A. a-graphene

Graphene is one of the miracle materials for nanoscale electronics nowadays because of its extremely high electron mobility, high Young's modulus, and large optical transmittance.[101,102] Hence, it is intriguing to investigate whether these properties are preserved in a-graphene. A recent study applied UV-vis spectroscopy characterizing the transmittance of a-graphene films grown under different substrate temperatures.[58] As shown in Fig. 4(a), a-graphene films show their high optical transmittance over 80% in the wavelength from 200 nm to 1000 nm. With increasing the processing temperature, the thickness of films is raised, which will reduce the optical transmittance accordingly. Under illumination of light source with a wavelength of 550 nm, the transmittance of a-graphene can be as high as 92.3%, which is superior to that of CVD grown crystalline graphene film with the same thickness.[103] On the other hand, the electrical properties of as-grown a-graphene films were characterized by fabricating into diodes.[58] The current–voltage ($I$–$V$) output characteristics show a linear relationship, implying an Ohmic contact at the electrode/a-graphene interface [Fig. 4(b)]. The electrical conductivity shows an increasing trend along with rising of growth temperature. It is worth noting that an a-graphene film prepared at 650 °C exhibits an insulating behavior as shown in the inset of Fig. 4(b), which could be explained by the poor continuity of the film. Further measurement shows that the conductivities of a-graphene films can be tenfold enhanced by nitrogen doping. The results of transmittance and $I$–$V$ characterization reveal the potential of a-graphene films for transparent electronic applications.

Owing to the high surface area and insulating behavior, a-graphene has been considered promising for the application in transformer oil (TO) nanofluids.[42] Dielectric strength and thermal conductivity are two significant figure-of-merits for transformer oil, which determine the ability against electrical stress and cooling performance, respectively.[104] Compared to the bare oil, the dielectric breakdown voltage is enhanced up to 40% as well as decreasing of dielectric loss by adding a-graphene in the nanofluids with a weight percentage of 0.0025 wt. % [Fig. 4(c)]. The reasons for such an enhancement can be explained by the polarization and relaxation of a-graphene as well as the moisture adsorption from oil.[42] In addition, the thermal conductivity of TO is boosted by 30% at the a-graphene concentration of ~0.01 wt. % due to the large surface area of the amorphous nanostructures. As shown in the thermal images [Fig. 4(d)], the temperatures of a-graphene nanofluids increase with the loading percentage of the nanostructures under

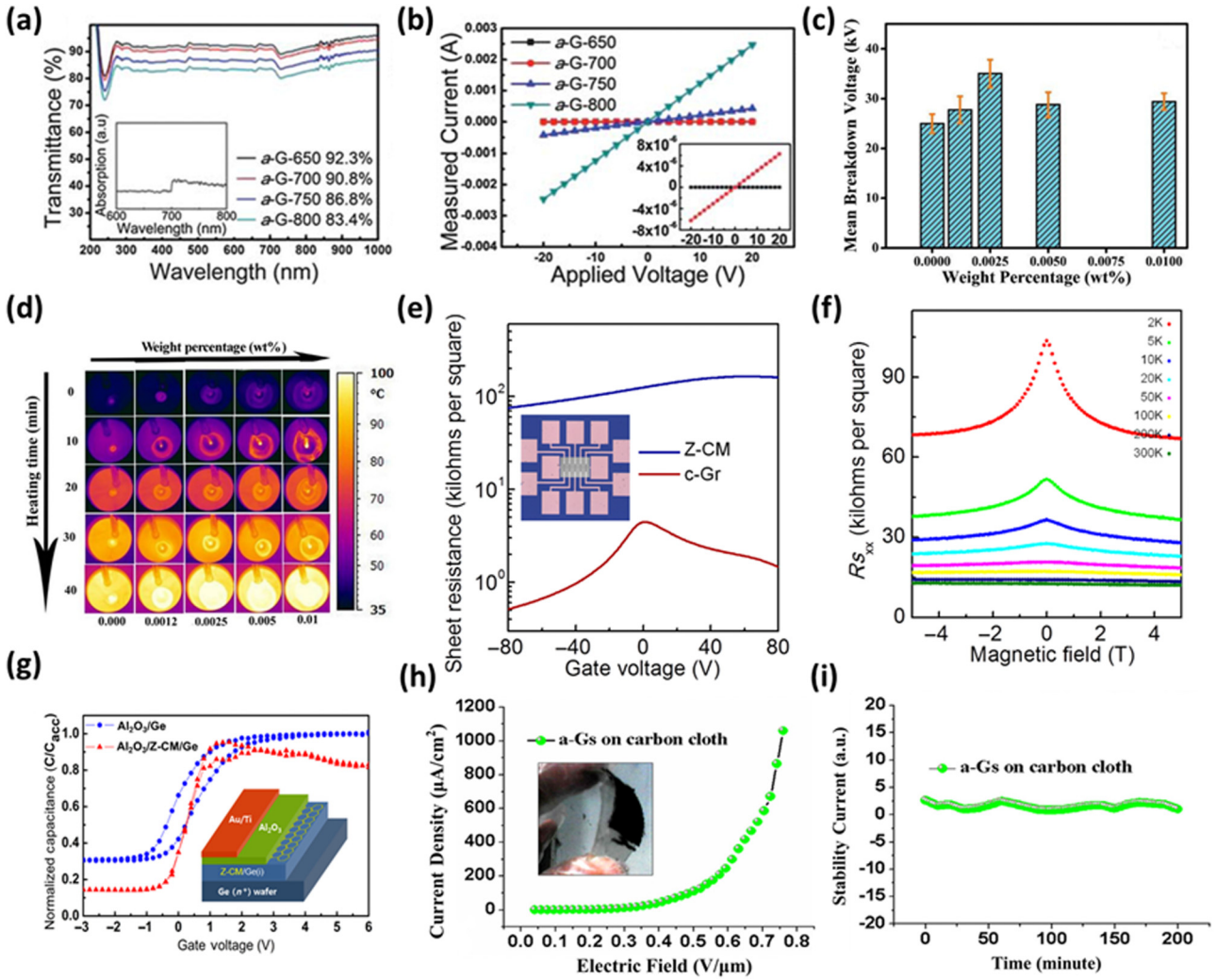


**FIG. 4.** Properties and applications of a-graphene. (a) Optical transmittance spectra of a-graphene films grown under different temperatures. Inset curve shows the absorption spectrum of the MgO substrate. (b) Output characteristics of a-graphene films grown under different temperatures. Inset shows the enlarged *I–V* curve of films grown under 650 °C and 700 °C, respectively. Reproduced with permission from Zhao *et al.*, J. Mater. Chem. **22**, 19679 (2012). Copyright 2012 The Royal Society of Chemistry. (c) The mean breakdown voltage of the nanofluid as a function of weight percentage of a-graphene. (d) The infrared images of bare oil and nanofluids as a function of heating time and weight percentage. Reproduced with permission from Bhunia *et al.*, Carbon **139**, 1010 (2018). Copyright 2018 Elsevier. (e) The curves of sheet resistances vs applied gate voltages for FETs based on Z-CM and crystalline graphene, respectively. Inset picture shows the electrode pattern of FETs. (f) The longitudinal sheet resistance of Z-CM FET as a function of applied magnetic field at different temperatures. (g) The normalized capacitance vs gate voltage curve of $Al_2O_3$/Ge and $Al_2O_3$/Z-CM/Ge, respectively. Inset shows the schematic image of MOS capacitor based on Z-CM. Reproduced with permission from Joo *et al.*, Sci. Adv. **3**, e1601821 (2017). Copyright 2017 AAAS. (h) The FE current density of a-graphene on the CC substrate as a function of applied electric field. Inset image shows the photograph of a-graphene/CC flexible field emitter. (i) The stability test of FE performance of a-graphene/CC field emitter. Reproduced with permission from Chattopadhyay *et al.*, Carbon **72**, 4 (2014). Copyright 2014 Elsevier.

identical heating time, implying that the heat transport is enhanced by the nanofluids. The outstanding dielectric properties and thermal conductivity make the a-graphene based nanofluid promising for optimizing the performance of electrical transformers.

2D carbon glass is a monolayer carbon film with continuous and random arrangement of atoms, which also belongs to the category of a-graphene.[105] Recently, an atomically thin wafer-scale carbon glass, Zachariasen carbon monolayer (Z-CM), was realized on a Ge substrate by CVD.[41] By fabricating into a field-effect transistor (FET), the sheet resistance of Z-CM was characterized as a function of gate voltages, exhibiting two orders of magnitude higher than that of crystalline monolayer graphene [Fig. 4(e)]. The

resistance of Z-CM dramatically increases when the temperature is below 50 K, showing the typical Anderson insulating behavior, which can be explained by the highly disordered structure. Moreover, due to its strong localized charge carriers, the magnetoresistance (MR) effect of Z-CM is strongly enhanced when decreasing the temperature, leading to a giant MR as high as 30% at 2 K [Fig. 4(f)]. In addition, the ultrathin thickness and inhomogeneous distribution of charge carriers enable Z-CM to be used as an interfacial layer for constructing heterostructures. In this study, a metal–oxide–semiconductor (MOS) capacitor based on Au (20 nm)/Ti (5 nm)/$Al_2O_3$ (15 nm)/Z-CM/Ge (110) has been fabricated and demonstrated optimized dielectric performance compared to an $Al_2O_3$/Ge based device [Fig. 4(g)]. A steep C–V curve without any hysteresis loop is shown thanks to the suppression of Ge oxidization, revealing the passivation function of the Z-CM layer.

Crystalline graphene is considered to possess excellent field emission (FE) properties owing to its atomic thickness, outstanding electrical conductivity, and good mechanical properties.[106] A recent work reported the FE characteristics of a-graphene and its hybrid structures, where a-graphene was realized by unzipping amorphous carbon nanotubes (a-CNTs).[39] According to the measurement results, the relationship between current density ($J$) and applied electric field ($E$) indicates that a-graphene not only shows very good FE performance itself in comparison with a-CNTs but also could effectively optimize the FE properties of the hybrid system containing a-graphene. Moreover, a-graphene was also realized on a flexible CC substrate to form a flexible field emitter [inset of Fig. 4(h)]. The FE current density of this flexible device is ~1050 $\mu$A/cm$^2$ at the electric field of 0.76 V/$\mu$m and exhibits a turn-on field as low as 0.52 V/$\mu$m, which is much lower than that of crystalline graphene related systems [Fig. 4(h)].[106,107] In addition, the stability test shows that the FE properties of a-graphene/CC field emitter are relatively stable over a period of 200 min. The excellent FE performance of an a-graphene based hybrid system may be ascribed to the sharp edges and the wrinkle, which could act as FE tips on the surface and suppress the screening effect. The above study suggests that a-graphene has a great potential for high-performance field emitting applications.

### B. a-$MoS_2$

In the post-graphene era, $MoS_2$ is a rising star in the 2D family because of its large tunable bandgaps, low cost, and high stability, which facilitate its considerable progress in the fields of energy storage, electronics, and conversion devices.[108,109] Recently, the highly disordered form of $MoS_2$ has been extensively studied as a complementary of crystalline counterpart.[37,67,90] One of the significant applications of a-$MoS_2$ is the hydrogen evolution reaction (HER) catalyst thanks to its highly intrinsic activity, large number of active sites, and low cost [Fig. 5(a)].[90,92,110] In contrast to crystalline $MoS_2$, the high HER performance of a-$MoS_2$ results from their short Mo–Mo and Mo–S bonds [inset of Fig. 5(b)].[43] As shown in Fig. 5(b), both a-$MoS_2$ and 1T-$MoS_2$, which also possesses a short bond structure, exhibit superior HER activity to that of 2H phase. Moreover, while the catalytic activity of 1T-$MoS_2$ gradually decreases over time, the performance of a-$MoS_2$ maintains with a high level in 24 h, showing an excellent stability of HER activity. The higher HER performance of a-$MoS_2$ can be explained by the larger intrinsic electronic conductivity induced by the short-range atomic order.

The HER activity of $MoS_2$ could be promoted by enhancing its conductivity via doping nanoparticles, edge modification, and integration with carbon materials.[92,111–113] Cao *et al.* have prepared a nanocomposite based on a-$MoS_2$ and highly conductive carbon black (CB) for HER characterization.[111] As illustrated in Fig. 5(c), the HER performance of different material systems, including CB, $MoS_2$-18, $MoS_2$-18/CB, $MoS_2$/CB-18, and commercial 20% Pt/C have been evaluated under same measurement conditions. It is worth noting that the composite of $MoS_2$/CB-18 exhibits excellent HER performance with an onset overpotential of only 78 mV and achieving current density of 470 mA/cm$^2$ at the overpotential of 200 mV, which is much superior to that of bare a-$MoS_2$ and even 1.5 times higher than that of commercial 20% Pt/C catalysts. Such intriguing HER activity results from the higher concentration and improved utilization of active sites caused by the amorphous structure and supported hydrophilic CB. More recently, Wang *et al.* optimized the a-$MoS_2$ electrocatalysts by fabricating a-$MoS_2$ films on Au/CC substrates, which could not only improve the HER activity of a-$MoS_2$ but also largely strengthen the stability of HER reaction owing to the strong interaction between a-$MoS_2$ and Au/CC.[92] According to the results of the cycling test with 5000 continuous cyclic voltammetry (CV) [Fig. 5(d)], both $MoS_2$/CC and $MoS_2$/Au/CC show excellent stability of HER performance, which are better than those of previously reported $MoS_2$ catalyst.[114] Meanwhile, the HER activity of $MoS_2$/Au/CC is more stable in comparison with $MoS_2$/CC after CV cycles, revealing that the Au layer could effectively enhance the adherent interaction between $MoS_2$ and CC substrate.

Besides combining with carbon materials, integration with nickel (Ni) composites could also result in better electrochemical performance. A recent study utilized a dendrite-like Cu on Ni foil (Cu@Ni–P) as a template for fabricating a-$MoS_2$ catalysts.[115] As shown in Fig. 5(e), the onset potential of Cu@Ni–P@a-$MoS_2$ (118.5 mV) is much superior to that of a bare Ni foil (197 mV) and several times smaller than that of other 2D materials.[119,120] Meanwhile, the Tafel slope of Cu@Ni–P@a-$MoS_2$ was extracted as 60.5 mV/dec, which is almost one-third of that from the bare Ni substrate. The fine HER performance of this a-$MoS_2$ composite attributes to its unique structure, which may provide more edge sites and large electrical conductivity of Cu and Ni. Table II summarizes the main figure-of-merit (FOM) of HER of a-$MoS_2$ obtained by different synthesis techniques. Among the various methods, the a-$MoS_2$ sample obtained by the hydrothermal process shows the lowest onset potential and Tafel slope, and highest exchange current density, which result from a large number of active sites and high intrinsic activity. On the other hand, although a-$MoS_2$ samples made by PLD, sputtering, and ALD exhibit inferior HER performance, the size of these films is relatively large, which is desirable for applications of HER catalysts.[110] Besides, Morales-Guio and Hu have applied an a-$MoS_2$ layer to promote the photoelectrochemical (PEC) HER performance of a photocathode based on $TiO_2$ protected $Cu_2O$ thin films [Fig. 5(f)].[116] The device generated photocurrents up to −5.7 mA/cm$^2$ at 0 V vs RHE with a ~100% Faradaic yield. Moreover, the $Cu_2O$–a-$MoS_2$ photocathode can

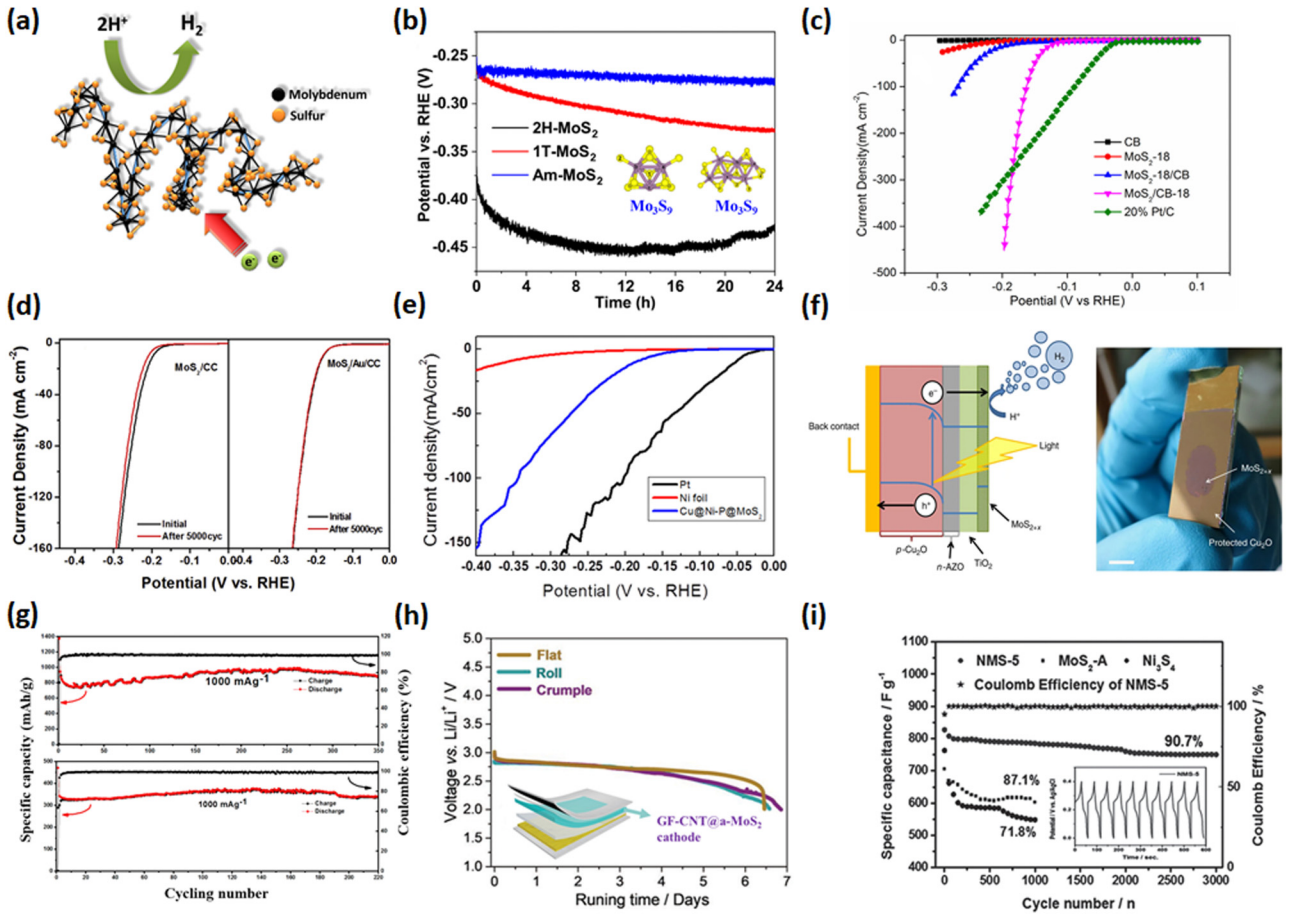


**FIG. 5.** Electrochemical properties and applications of a-$MoS_2$. (a) Schematic of HER process of a-$MoS_2$. Reproduced with permission from Morales-Guio and Hu, Acc. Chem. Res. **47**, 2671 (2014). Copyright 2014 American Chemical Society. (b) The potential vs RHE as a function of time for $MoS_2$ with different phases. Inset shows the atomic structure of a-$MoS_2$ clusters. Reproduced with permission from Wu *et al.*, ChemSusChem **12**, 4383 (2019). Copyright 2019 Wiley-VCH. (c) Cathodic polarization results of different materials, including CB, $MoS_2$-18, $MoS_2$-18/CB, $MoS_2$/CB-18, and 20% Pt/C. Reproduced with permission from Cao *et al.*, J. Power Sources **347**, 210 (2017). Copyright 2017 Elsevier. (d) The LSV polarization curves for both a-$MoS_2$/CC and a-$MoS_2$/Au/CC before and after 5000 cycles, respectively. Reproduced with permission from Wang *et al.*, Electrochim. Acta **258**, 876 (2017). Copyright 2017 Elsevier. (e) Polarization curves of different catalysts, including Pt, Ni foil and Cu@Ni–P@a-$MoS_2$. Reproduced with permission from Ahn *et al.*, Appl. Surf. Sci. **432**, 183 (2018). Copyright 2018 Elsevier. (f) Left: Schematic of the working mechanism of a-$MoS_{2+x}$–$Cu_2O$ photocathode. Right: Photograph of the a-$MoS_{2+}$–$Cu_2O$ photocathode. Reproduced with permission from Morales-Guio *et al.*, Nat. Commun. **5**, 3059 (2014). Copyright 2014 Nature Publishing Group. (g) Long-term cycling performance of the electrode for both LIBs (up) and SIBs (down) at 1000 mA/g, respectively. Reproduced with permission from Zhu *et al.*, ACS Sustainable Chem. Eng. **5**, 8025 (2017). Copyright 2017 American Chemical Society. (h) Discharging voltages as a function of running time for a flexible Li–$O_2$ battery under different states. Inset image shows the schematic of the flexible battery using GF-CNT@a-$MoS_2$ as the cathode. Reproduced with permission from Song *et al.*, Small Methods, 1900274 (2019). Copyright 2019 Wiley-VCH. (i) Long-term cycling performance of different materials, including $Ni_3S_4$@a-$MoS_2$, a-$MoS_2$, and $Ni_3S_4$ at 10 A/g. The inset shows the last ten cycles of $Ni_3S_4$@a-$MoS_2$. Reproduced with permission from Zhang *et al.*, Small **11**, 3694 (2015). Copyright 2015 Wiley-VCH.

efficiently work under both acid and slightly normal conditions, which also exhibits remarkable PEC hydrogen evolution, demonstrating a promising device for solar hydrogen production.

In addition to catalysts for HER, a-$MoS_2$ based materials also found applications for energy storage thanks to their excellent electrochemical properties.[68,117,118] Recently, an amorphous composite based on a-$MoS_2$/$MoO_3$/nitrogen-doped carbon (n-C) has been fabricated as electrodes for both sodium ion batteries (SIBs) and lithium ion batteries (LIBs).[117] According to the results of electrochemical cycling test, the discharge specific capacity of the 50th cycle of LIBs based on a-$MoS_2$ composites is obtained as high as 1253.3 mAh/g under the current density of 100 mA/g, which is almost fourfold greater than that of commercial graphite electrode (372 mAh/g). Moreover, at the current density of 1000 mA/g, the electrode can still attain 887.5 mAh/g after 350 cycles [Fig. 5(g)]. In the same way, the electrochemical performance of SIBs with

**TABLE II.** Summary of HER parameters of a-$MoS_2$ based electrochemical catalysts.

| Catalyst | Fabrication method | Onset potential (mV) | Tafel slope (mV $dec^{-1}$) | $j_0$ ($\mu A\ cm^{-2}$) | References |
|---|---|---|---|---|---|
| a-$MoS_2$ | Electro-polymerization | 150 | 40 | 0.13 | 121 |
| a-$MoS_2$/CB-18 | Hydrothermal process | 78 | 39 | 36 | 111 |
| a-$MoS_2$/CC | Magnetron sputtering | 177 | 58 | … | 90 |
| a-$MoS_2$/Au/CC | PLD | 132 | 48 | 1.7 | 92 |
| Cu@Ni–P@a-$MoS_2$ | Thermolysis | 118.5 | 60.5 | … | 115 |
| a-$MoS_2$/Au | ALD | 165 | 47 | 0.027 | 67 |

a-$MoS_2$ composite as anode was characterized, exhibiting a large discharge specific capacity of 538.7 mAh/g after 200 cycles at a current density of 300 mA/g. For a long-term test at 1000 mA/g, the a-$MoS_2$ SIBs can achieve a discharge specific capacity up to 339.9 mAh/g after 220 cycles. Interestingly, the Coulombic efficiencies of both LIBs and SIBs almost maintain 100% within the entire long-term test, revealing an excellent long-term cycling stability with the electrode of an a-$MoS_2$ composite [Fig. 5(g)]. Compared to LIBs, Li–$O_2$ batteries (LOBs) are known for higher capacity but with poorer cycling stability and suffer from the large voltage hysteresis between charge and discharge.[122] Previous studies have shown that the highly disordered $MoS_2$ nanoparticles could effectively improve the oxygen reduction reaction (ORR) and oxygen evolution reaction (OER) activities.[123] Considering this effect, Song *et al.* demonstrated a new cathode material for LOBs, which is prepared by depositing a-$MoS_2$ film on the 3D graphite foam supported carbon nanotube substrate (GF-CNT@$MoS_2$).[68] The obtained LOBs not only exhibit high capacity of 4844 mAh/g and high energy efficiency of 83%, but also have a long-term cycle life up to 190. Both theoretical calculation and experimental results verify that the improved energy storage performance ascribes to the increased active catalytic sites from the non-crystalline structure of a-$MoS_2$. Furthermore, thanks to the outstanding flexibility of the GF-CNT@a-$MoS_2$ cathode, a wearable Li-air battery (LAB) was demonstrated as shown in the inset of Fig. 5(h). The discharging voltages of flat, roll, or crumple states of LAB maintain nearly unchanged for more than six days [Fig. 5(h)], suggesting that a-$MoS_2$ based composites could be a potential candidate for flexible energy storage devices.

Different from rechargeable batteries, supercapacitors (SCs) aim at electrical applications that require rapid charging/discharging rate rather than long-term storage.[124] Considering the high electrical conductivity and electrochemical stability of a-$MoS_2$, Zhang *et al.* have synthesized a core/shell structure based on $Ni_3S_4$ and a-$MoS_2$ for SCs application by a facile hydrothermal method.[118] The size of the core and shell structure can be accurately controlled by the ratios of precursors. The electrochemical measurement shows that $Ni_3S_4$@a-$MoS_2$ electrode possesses a large capacitance of 1440 F/g at a current density of 2 A/g, which is much superior to those of $Ni_3S_4$ nanoparticles and a-$MoS_2$ nanospheres (1226.5 F/g and 742.8 F/g at 2 A/g, respectively), exhibiting an excellent performance as the electrodes of SCs. In addition, the cycling performance of $Ni_3S_4$@a-$MoS_2$ preserves as high as 90.7% specific capacitance after 3000 cycles while the Coulomb efficiency is nearly 100% within the whole test, indicating good long-term stability of SCs based on a-$MoS_2$ composites [Fig. 5(i)].

Besides the electrochemical applications, 2D a-$MoS_2$ has also drawn a lot of interest for optoelectronic applications owing to its unique structure and efficient light absorption.[37,125] Interestingly, a lateral photovoltaic (LPV) effect was investigated in an a-$MoS_2$/Si junction prepared by the PLD method.[125] According to the results of longitudinal $I$–$V$ characterization, the a-$MoS_2$/p-Si and a-$MoS_2$/n-Si junctions show different orientations in terms of breakover voltages and built-in field, leading to tunable LPV performance. As shown in Fig. 6(a), the LPV of both a-$MoS_2$/p-Si and a-$MoS_2$/n-Si junctions exhibit good linear relationship on the position of illumination. Large positional sensitivities of 183 and 145 mV/mm were obtained for a-$MoS_2$/p-Si and a-$MoS_2$/n-Si, respectively. The higher sensitivity of a-$MoS_2$/p-Si is attributed to the smaller recombination rate of photocarriers in p-Si compared to n-Si substrates. In addition, a strong variation of time response of LPV was observed between a-$MoS_2$/p-Si and a-$MoS_2$/n-Si as well [Figs. 6(b) and 6(c)]. The LPV relaxation time of a-$MoS_2$/n-Si junction is obtained as 5.8 $\mu$s, which is around threefold than that of p-Si based junction (2.1 $\mu$s), exhibiting ultrafast relaxation of LPV. The wafer-scale device and promising LPV performance enable a-$MoS_2$ based on junction in favor of fast position-sensitive sensors.

Due to numerous defects, 2D a-$MoS_2$ has a narrow bandgap of 0.196 eV, which makes it suitable for broadband photodetection.[37] Recently, Huang *et al.* developed an a-$MoS_2$ based photodetector by the PVD method [Fig. 6(d)]. An ultrabroadband photoresponse ranging from 473 to 2712 nm was observed [Fig. 6(e)], which is much broader than those of traditional InGaAs (800–1700 nm) and crystalline $MoS_2$ photodetectors (850–1550 nm).[37,126] With an increase in the wavelength, photoresponsivity ($R_\lambda$) and detectivity ($D^*$) of a 114.5 nm thick a-$MoS_2$ film show same trend with achieving peak values of 16 mA/W and $1.26 \times 10^7$ Jones at a wavelength of 520 nm, respectively. Moreover, the response time of a-$MoS_2$ photodetector was obtained as 10 ms [Fig. 6(f)], which is superior to that of 2D $MoS_2$ device even with encapsulation layer.[127] The broadband photodetection of a-$MoS_2$ will widen its applications in the field of optoelectronics for communication, imaging, and sensor applications. In summary, the non-crystalline structure makes 2D a-$MoS_2$ exhibiting outstanding electrochemical properties and distinctive optoelectronic performance. Considering the scalable, low-cost, and facile fabrication methods, a-$MoS_2$ would be a potential choice for future industrial applications.

### C. a-BN

Owing to excellent insulating property and graphene-like structure, 2D hexagonal BN has emerged as one of promising

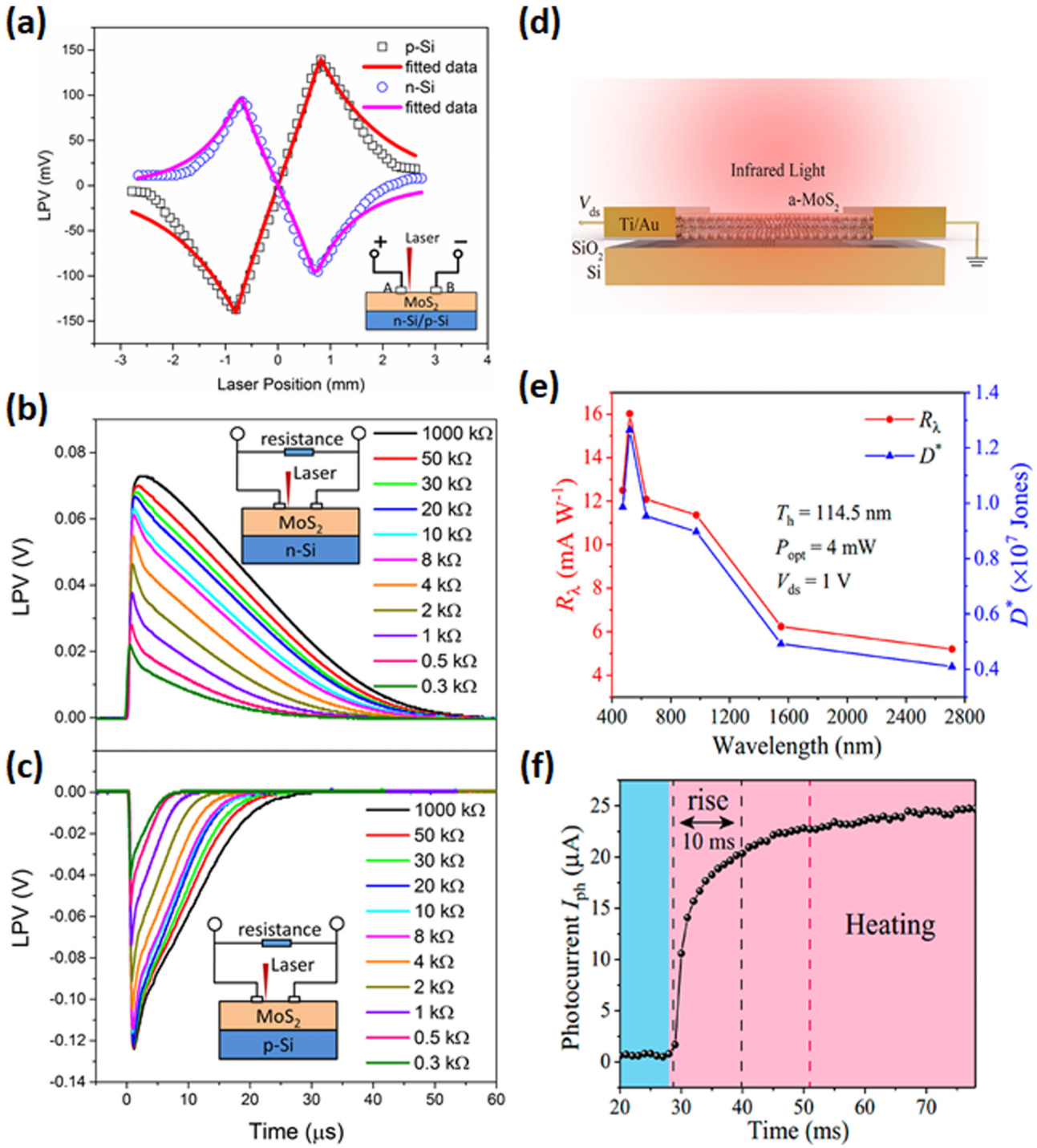


**FIG. 6.** Optoelectronic applications of a-$MoS_2$. (a) The LPV of a-$MoS_2$/p-Si and a-$MoS_2$/n-Si as a function of illumination positions. The inset image shows schematic of a-$MoS_2$/Si junction. (b) and (c) The LPV of a-$MoS_2$/n-Si and a-$MoS_2$/p-Si junctions as a function of time. The inset shows the schematic circuits of the test. Reproduced with permission from Hu *et al.*, ACS Appl. Mater. Interfaces **9**, 18362 (2017). Copyright 2017 American Chemical Society. (d) Schematic image of an a-$MoS_2$ photodetector under illumination of infrared light. (e) The photoresponsivity and detectivity of a-$MoS_2$ photodetector as a function of wavelength. (f) Temporal response of a-$MoS_2$ photodetector at $V_{ds}$ = 1 V. The obtained rise time is 10 ms. Reproduced with permission from Huang *et al.*, ACS Appl. Electron. Mater. **1**, 1314 (2019). Copyright 2019 American Chemical Society.

dielectric substrates for 2D electronics.[128,129] Compared to crystalline BN, the amorphous counterpart exhibits comparable dielectric properties as well as mild synthesis temperature, which makes it potential for flexible dielectric applications.[130] As discussed above, ultrathin large-area a-BN films have been realized on various substrates at low temperature (<200 °C) by PLD.[46] The electrical and dielectric properties of the films were characterized to test the applicability of wafer-scale and device production. As shown in Fig. 7(a), the a-BN film was utilized as an active resistor in an electrical device with back-gated configuration. A dense and uniform a-BN layer can be observed from the cross-sectional TEM image of the device [Fig. 7(b)]. Along with an increase of film thickness from 2 nm to 16.5 nm, the resistivity values are changed from $\sim 10^6\,\Omega$ cm to $\sim 3\times 10^{12}\,\Omega$ cm, which are near the expected values of hexagonal BN ceramics.[131] Moreover, the dielectric constants as a function of frequency were measured for a-BN films with different thicknesses. As shown in Fig. 7(c), the obtained dielectric constants for 6.0 nm and 16.5 nm thick a-BN film are 5.2 and 6.5 at 1 kHz, respectively, which is almost twofold than that of the CVD grown polycrystalline h-BN film.[132] Meanwhile, the dielectric breakdown voltage is obtained as 9.1 MV/cm, demonstrating a superior strength compared to traditional 2D dielectrics.[133] The excellent dielectric performance of the a-BN film may result from its large electrical resistivity.

Recently, low-power resistive switching (RS) memory based on 2D materials have attracted much attention.[134,135] Thanks to the promising insulating properties and high thermal conductivity, a-BN films have been utilized to fabricate conductive bridging random access memory (CBRAM) with improved resistive switching (RS) performance.[136] In this work, an a-BN layer was inserted between Ag and Pt films, which serve as top and bottom electrodes, respectively. Figure 7(d) presents the RS characteristics of a-BN CBRAM devices in pristine states, which are in either low-resistance state (LRS) or high resistance state (HRS) depending on the thickness of the a-BN layer. The variation of film thickness strongly influences the diffusion amount of Ag in a-BN, which further leads to different initial resistance states. According to the stability test, all 5.5 nm thick a-BN devices (M1) are in LRS thanks to the large amount diffusion of Ag ions. On the other hand, the reduced amount of diffused Ag in 21.5 nm thick a-BN films (M3)

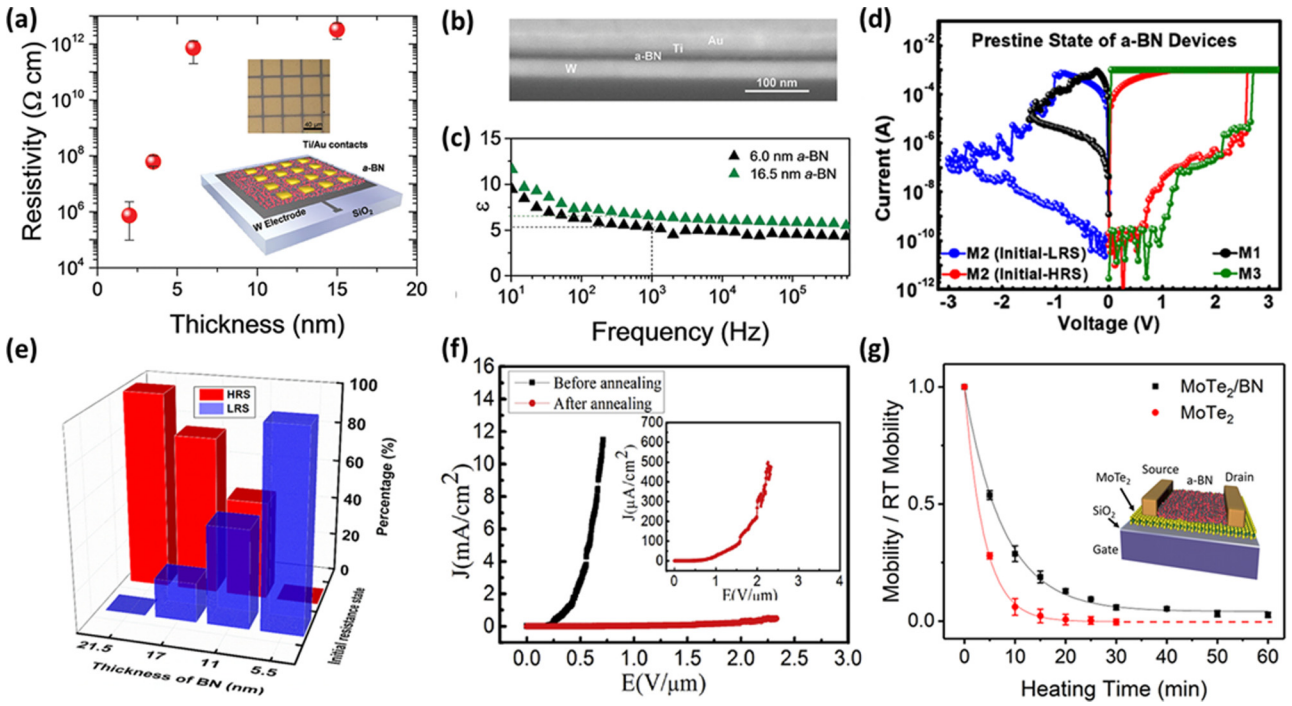


**FIG. 7.** Properties and applications of ultrathin a-BN films. (a) The resistivity of a-BN device as a function of thickness. Inset shows the pattern of electrode contacts and the schematic of a-BN resistor. (b) Cross-sectional TEM image of a-BN device. (c) The characterization of dielectric constants of a-BN films with different thicknesses. Reproduced with permission from Glavin *et al.*, Adv. Funct. Mater. **26**, 2640 (2016). Copyright 2016 Wiley-VCH. (d) RS behaviors of a-BN CBRAMs in pristine states. M1, M2, and M3 samples are devices based on a-BN with thickness of 5.5, 11, and 21.5 nm, respectively. (e) Statistic bars of RS performance as a function of thickness of a-BN. Reproduced with permission from Jeon *et al.*, ACS Appl. Mater. Interfaces **11**, 23329 (2019). Copyright 2019 American Chemical Society. (f) The plot of J–E of a-BN film before and after annealing. Inset shows the enlarged curve of annealing film. Reproduced with permission from Li *et al.*, J. Alloys Compd. **705**, 734 (2017). Copyright 2017 Elsevier. (g) The normalized mobility of FETs based on a-BN covered and uncovered $MoTe_2$ as a function of heating time at 100 °C in ambient. Inset shows the schematic image of a-BN protected $MoTe_2$ FET. Reproduced with permission from Sirota *et al.*, Sci. Rep. **8**, 8668 (2018). Copyright 2018 Nature Publishing Group.

leads to HRS in every M3 device [Fig. 7(e)]. In addition to the initial states, further RS characteristics show bipolar switching behavior with RESET at negative bias and SET at positive bias, respectively. The current switching ratio has been found appreciably enlarged along with increasing of a-BN thickness. This work suggests that a-BN CBRAM is programmable for films with appropriate thickness.

Because of the wide bandgap, 2D BN has also been considered for the application of FE source due to the negative electron affinity (NEA).[137] Recently, the FE properties were investigated in ultrathin a-BN films prepared by PECVD.[65] As shown in Fig. 7(f), the FE current density of an a-BN film before annealing is more than two orders higher compared to the annealed film, indicating that highly disordered BN has better FE performance than that of the crystalline phase. According to the measurement results, the current density of non-annealed a-BN film achieves 12 mA/cm$^2$ when the applied field is only 0.75 V/$\mu$m, and the turn-on field, which is defined as the minimum demand field to generate 1 $\mu$A/cm$^2$, is extracted as low as ~0.5 V/$\mu$m. The excellent FE performance of a-BN films is attributed to its unique mixed amorphous structure embedded with nanocrystals, which results in the efficient electron step-transport in various energy states and multi-channel transportation of carriers at the boundary between nanocrystals and a-BN.

Besides the above applications, a-BN is also favorable to be used as a passivation layer for other 2D materials, which could effectively protect the ultrathin 2D layers from the chemical oxidation and optimize the device performance.[83,138] A representative work is conducted by Sirota and co-workers, demonstrating that the durability of $MoTe_2$ FET was significantly improved by a 10 nm thick a-BN film prepared by PLD.[138] As shown in Fig. 7(g), the normalized mobility of both a-BN capped and uncapped $MoTe_2$ FETs decrease with flowing time after the devices heating to 100 °C in air. The mobility of uncovered device shows a higher decreasing speed in comparison with that of a-BN/$MoTe_2$, revealing that integration with a-BN film could effectively preserve the electronic performance under high temperature. Meanwhile, it should be noticed that the mobility of uncapped $MoTe_2$ FET is too small to be detected after 30 min. On the other hand, a-BN/$MoTe_2$ device could maintain a long-term performance over 60 min, which verifies an optimized durability with the protection of an a-BN film.

### D. a-BP

The research interest in phosphorene is continuously growing since its first isolation from bulk BP in 2014.[13,85] Thanks to its layered structure, crystalline BP shows tunable direct bandgaps from 0.3 eV to ~2.0 eV and can just bridge the gap between graphene and 2D $MoS_2$,[12] which makes it favorable for broadband nano-optoelectronic devices in infrared region.[139,140] Similar to crystalline 2D BP, the PLD grown highly disordered BP thin films also possess thickness dependent bandgaps.[38] As shown in Fig. 8(a), the optical bandgap of a 2 nm thick a-BP thin film is around 0.8 eV according to the photoluminescence (PL) spectrum. Meanwhile, the optical absorption spectrum indicates that the estimated bandgaps of an 8 nm thick a-BP film are in a range from 0.21 eV to 0.26 eV. Thus, along with the thickness increasing from 2 nm to 8 nm, the bandgaps of a-BP thin films are significantly reduced, which is consistent with the variation tendency of crystalline 2D BP.[141,142]

Besides the optical properties, the photocarrier dynamics of a-BP thin films have also been studied by Zhao *et al* in collaboration with our team.[137,143] The transient reflection measurements were carried out on a 2 nm film by an ultrafast pump-probe spectroscopy system. According to Fig. 8(b), the differential reflection signals rapidly increase to the peak value within 1 ps delay time as a typical thermalization process and then exponentially decrease to a saturated level. The lifetime of a BP exciton (~400 ± 20 ps) can be extracted from the double exponential fitting of the decay process. Furthermore, the transport properties of BP excitons were studied by a spatially resolved differential reflection measurement [Fig. 8(c)]. The 2D diffusion of the excitons can be clearly observed. The Gaussian function is applied to fit the transport signal of a-BP excitons, resulting in the diffusion coefficient of ~5.3 ± 0.5 cm$^2$ s$^{-1}$, which is much superior to other amorphous semiconductors. The long lifetime and large diffusion coefficient confirm good charge transport properties in ultrathin a-BP thin films.

Moreover, a 2D heterostructure was constructed based on an a-BP thin film and monolayer $WS_2$ to investigate the interlayer charge transfer process.[144] Integration of materials with different crystalline structures could give rise to some novel properties and expand the application scope. The charge or energy transfer from the $WS_2$ layer to a-BP in the heterostructure is evidenced by the significant quenching of a $WS_2$ PL signal. To further clarify the mechanism, the photocarrier dynamics of the heterostructure were studied by a transient reflection measurement. As shown in Fig. 8(d), no signal is observed for a-BP film since the probe photon energy is much larger than its bandgap. At the same time, the differential reflection signal of the $WS_2$/a-BP heterostructure is much smaller and decays at a slower rate than that of a sole $WS_2$ nanosheet, verifying that holes can effectively transferred from a monolayer $WS_2$ to an a-BP film with an ultrafast time scale (<100 fs). Further study also rules out the possibility of electron transfer at the interface owing to the localized electronic states in an a-BP film. The results validate that electrical connections can be constructed between a-BP and other 2D materials.

In the field of electronics, a large-area 2D a-BP film has been fabricated into FET based on the back-gate configuration.[38] Ohmic contact is achieved at the interface of electrode/a-BP. As shown in Fig. 8(e), a typical p-type semiconducting behavior can be observed from the transfer curve of a-BP FET. The field-effect mobility and on/off ratio are extracted from the $I_d$–$V_g$ curve as high as 14 cm$^2$ V$^{-1}$ s$^{-1}$ and $10^2$, respectively. The mobility of a-BP FET is much superior to those of other ultrathin amorphous films. Moreover, similar to crystalline BP,[13,86] the transport properties of a-BP can be modulated by the film thickness. Along with thickening of a-BP film from 2 to 10 nm, the mobility gradually increases from 14 to ~$10^2$ cm$^2$ V$^{-1}$ s$^{-1}$ while the switching ratio is significantly reduced around two orders owing to the screening effect and decreasing of the bandgaps [Fig. 8(f)]. Considering the large-scale, sizable bandgaps and high mobility, the a-BP film could be a potential candidate for high-performance electronic devices.

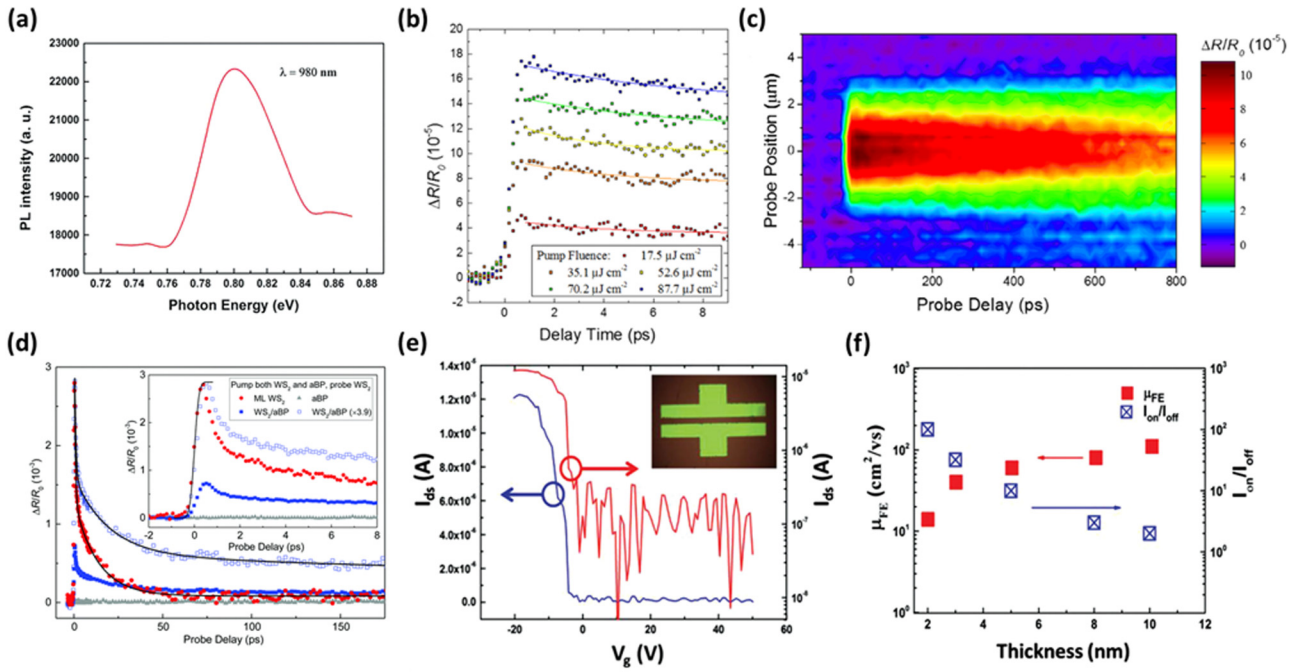


**FIG. 8.** Properties characterization and device demonstration of an a-BP film. (a) Photoluminescence spectrum of an ultrathin a-BP film with an excitation of 980 nm laser. (b) Differential reflection curve of 2 nm thick a-BP film excited by laser pulses with different pump fluences. (c) The spatiotemporal differential reflection signals obtained from a 2 nm thick a-BP film, presenting the diffusion profile of the excitons. Reproduced with permission from Bellus *et al.*, 2D Mater. **4**, 025063 (2017). Copyright 2017 IOP Publishing. (d) The differential reflection signals obtained from monolayer $WS_2$, a-BP, and $WS_2$/a-BP heterostructures, respectively. The blank square symbols show the magnified signal for better comparison. The inset curve shows the signal of early delay time. Reproduced with permission from Bellus *et al.*, Nanoscale Horiz. **4**, 236 (2019). Copyright 2019 The Royal Society of Chemistry. (e) The $I_{ds}$–$V_g$ curve of a-BP FET, exhibiting the transport properties of an a-BP film. The inset image shows the optical image of electrode pattern. (f) The field-effect mobility and on/off ratio of a-BP FET as a function of film thickness. Reproduced with permission from Yang *et al.*, Adv. Mater. **27**, 3748 (2015). Copyright 2015 Wiley-VCH.

## IV. ADVANTAGES AND MECHANISM OF 2D AMORPHOUS MATERIALS

Ever since the discovery of graphene, 2D layered materials have drawn much attention because of their remarkable properties, especially for the crystalline ones. However, the recent works have shown that the non-crystalline counterparts cannot be neglected since they possess their own featured properties and application scope.[27] Due to short of long-range atomic order, amorphous materials have more defects and impurities, which provide a large number of active sites and transport paths of charge carriers. Meanwhile, amorphous materials can be grown at a relatively low temperature and the cost is lower than those crystalline films, which make them favorable to industrial applications.

By introducing atomic disorder into the configuration of 2D materials, 2D amorphous materials combine the advantages from both the non-crystalline feature and ultrathin 2D structure, resulting in distinct properties. As shown in Table III, because of the abundant active sites and large surface area, 2D amorphous materials,

**TABLE III.** Summary of featured properties and applications of amorphous 2D inorganic materials.

| Materials | Featured Properties | Applications | References |
|---|---|---|---|
| a-graphene | Over 80% optical transmittance in 200–1000 nm, insulating behavior, high surface area | Transparent electronic devices, TO nanofluids, field emitter | 42, 58, and 106 |
| a-$MoS_2$ | Highly intrinsic activity, outstanding electrochemical property, good light absorption ability, narrow bandgap | HER, sodium and lithium ion batteries, photovoltaic devices, broadband photodetector | 37, 68, 92, and 125 |
| a-BN | Good dielectric properties, wide bandgap | CBRAM, FE devices, passivation layer | 46, 136, and 138 |
| a-BP | Tunable bandgap, good electrical properties | Flexible electronic devices | 38 |

such as a-$MoS_2$, are desirable for catalysts and energy storage applications. The defects could also depress the optical bandgaps of materials, which enables 2D amorphous materials applicable for broadband photodetection applications. Moreover, 2D amorphous materials usually have excellent mechanical properties and high transparency benefited from the ultrathin thickness, making them become potential candidates for flexible transparent devices. Furthermore, since 2D amorphous materials have a similar atomic structure to the crystalline counterpart but with randomly distributed stacks, they could also preserve several outstanding properties. For instance, a-BP nanosheets can not only be grown in large-area at low temperature but also exhibit tunable optical bandgaps and large carrier mobility, which is similar to phosphorene. These attractive features endow them with great potential for developing flexible electronic devices. To sum up, the unique structure and novel properties enable 2D amorphous materials to act as a significant complementary of their crystalline counterparts.

## V. CONCLUSION AND OUTLOOK

The advances of research studies on 2D materials have motivated extensive explorations to investigate the properties and potential applications of amorphous 2D materials. The short-range atomic order and 2D structure enable amorphous 2D materials to exhibit distinctive features relative to the crystalline phase. In this perspective, the recent progress of 2D amorphous inorganic materials, including a-graphene, a-$MoS_2$, a-BN, and a-BP has been overviewed in terms of synthesis, properties, and applications. First, the mechanism and structural characterizations of amorphous inorganic 2D materials prepared by either the CVD or PVD method have been summarized, illustrating that the scalable growth can be realized with low cost and facile fabrication conditions. Furthermore, the properties and proof-of-concept applications based on typical amorphous 2D materials are illustrated. Not only preserving some characteristics of crystalline counterpart, amorphous 2D materials also possess more active sites and easy transfer tunnels for electrons thanks to their non-crystalline structure and modified bandgap, which make them favorable for catalysis, energy storage, electronic, and optoelectronic applications. Additionally, the high stability in ambient and good dielectric properties suggest that this group of materials may serve as encapsulating layers for the ultrathin 2D candidates.

Currently, the research on amorphous 2D materials is still in the early stage relative to crystal ones. There are many issues of challenges and opportunities available to expand the properties and potential applications of amorphous 2D family. We select some of them as follows.

1. Over the past 10 years, hundreds of 2D layered materials have been discovered. In comparison with crystalline counterparts, the number of reported amorphous 2D materials is quite few. According to the previous discussion, it is known that CVD and PVD are two common methods to synthesize high quality 2D material, which make it possible to achieve the amorphous 2D material not yet discovered. Besides, the study on heterostructures of amorphous 2D materials is rarely reported so far. Continuous research should be carried out to create new heterostructures based on different 2D materials with either crystalline or amorphous structure, which may give rise to some unprecedented properties, such as distinct carrier transport and exciton behaviors in the novel heterostructures.
2. The mechanisms of synthesizing amorphous 2D materials are not very clear yet. Unlike crystalline materials, the growth of amorphous materials is not constrained by lattice mismatch. Thus, the reason for the formation of a 2D structure is not well understood. Up to now, relevant research is restricted for lack of the theoretical model to fully understand the amorphous 2D materials. More efforts should be made to investigate the growth mechanism both experimentally and theoretically in the future. Moreover, during the fabrication of amorphous 2D materials, nano-crystals and clusters with uncontrollable size and topology may be formed, which largely affect the properties of products. The principles to block the nucleation should be further explored.
3. The application scope of amorphous 2D family is still narrow relative to crystalline 2D materials. At present, many studies are mainly focused on the catalysis and energy storage applications by considering the amorphous structure. According to the above discussion, amorphous 2D materials possess numerous characteristics, which could drive the development of new applications. For instance, the tunable bandgaps, high uniformity, and large area suggest that a-BP could be utilized in the optoelectronic applications. Meanwhile, the expansion of amorphous 2D group and development of heterostructure will also broaden the application range.

The rise of amorphous 2D materials starts a new research area as an indispensable complement for 2D studies. Considering the facile fabrication conditions and low cost, it is foreseen that further advances in the synthesis and device demonstration of amorphous 2D materials and their heterostructure would potentially lead to practical devices in the future.

## ACKNOWLEDGMENTS

This work was supported by the National Natural Science Foundation of China (No. 51972279) and the Research Grants Council (RGC) of Hong Kong (Project Nos. PolyU 153271/16P, PolyU 153039/17P, and PolyU 153023/18P).

## DATA AVAILABILITY

The data that support the findings of this study are available from the corresponding author upon reasonable request.

## REFERENCES

[1]K. S. Novoselov, A. Mishchenko, A. Carvalho, and A. H. Castro Neto, Science **353**, aac9439 (2016).
[2]S. Z. Butler, S. M. Hollen, L. Cao, Y. Cui, J. A. Gupta, H. R. Gutiérrez, T. F. Heinz, S. S. Hong, J. Huang, A. F. Ismach, E. Johnston-Halperin, M. Kuno, V. V. Plashnitsa, R. D. Robinson, R. S. Ruoff, S. Salahuddin, J. Shan, L. Shi, M. G. Spencer, M. Terrones, W. Windl, and J. E. Goldberger, ACS Nano **7**, 2898 (2013).
[3]H. Zhang, M. Chhowalla, and Z. Liu, Chem. Soc. Rev. **47**, 3015 (2018).
[4]M. Chhowalla, D. Jena, and H. Zhang, Nat. Rev. Mater. **1**, 16052 (2016).
[5]X. Zhang, L. Hou, A. Ciesielski, and P. Samorì, Adv. Energy Mater. **6**, 1600671 (2016).

[6]Z. Yang, W. Jie, C.-H. Mak, S. Lin, H. Lin, X. Yang, F. Yan, S. P. Lau, and J. Hao, ACS Nano **11**, 4225 (2017).
[7]K. S. Novoselov, V. I. Fal'Ko, L. Colombo, P. R. Gellert, M. G. Schwab, and K. Kim, Nature **490**, 192 (2012).
[8]C. T. Phare, Y. H. Daniel Lee, J. Cardenas, and M. Lipson, Nat. Photonics **9**, 511 (2015).
[9]D. Jariwala, V. K. Sangwan, L. J. Lauhon, T. J. Marks, and M. C. Hersam, ACS Nano **8**, 1102 (2014).
[10]M. Chhowalla, H. S. Shin, G. Eda, L. J. Li, K. P. Loh, and H. Zhang, Nat. Chem. **5**, 263 (2013).
[11]Q. H. Wang, K. Kalantar-Zadeh, A. Kis, J. N. Coleman, and M. S. Strano, Nat. Nanotechnol. **7**, 699 (2012).
[12]X. Ling, H. Wang, S. Huang, F. Xia, and M. S. Dresselhaus, Proc. Natl. Acad. Sci. U. S. A. **112**, 4523 (2015).
[13]L. Li, Y. Yu, G. J. Ye, Q. Ge, X. Ou, H. Wu, D. Feng, X. H. Chen, and Y. Zhang, Nat. Nanotechnol. **9**, 372 (2014).
[14]Z. Yang and J. Hao, Adv. Mater. Technol. **4**, 1900108 (2019).
[15]W. Jie, X. Chen, D. Li, L. Xie, Y. Y. Hui, S. P. Lau, X. Cui, and J. Hao, Angew. Chem. Int. Ed. **54**, 1185 (2015).
[16]Q. Wei and X. Peng, Appl. Phys. Lett. **104**, 251915 (2014).
[17]J. Pu, Y. Yomogida, K.-K. Liu, L.-J. Li, Y. Iwasa, and T. Takenobu, Nano Lett. **12**, 4013 (2012).
[18]Y. Zhang, W. Jie, P. Chen, W. Liu, and J. Hao, Adv. Mater. **30**, 1707007 (2018).
[19]J. Hao and C. N. Xu, MRS Bull. **43**, 965 (2018).
[20]W. Jie, Z. Yang, G. Bai, and J. Hao, Adv. Opt. Mater. **6**, 1701296 (2018).
[21]Y. Saito, T. Nojima, and Y. Iwasa, Nat. Rev. Mater. **2**, 16094 (2016).
[22]C. Zheng, L. Yu, L. Zhu, J. L. Collins, D. Kim, Y. Lou, C. Xu, M. Li, Z. Wei, Y. Zhang, M. T. Edmonds, S. Li, J. Seidel, Y. Zhu, J. Z. Liu, W. X. Tang, and M. S. Fuhrer, Sci. Adv. **4**, eaar7720 (2018).
[23]S. Yuan, X. Luo, H. L. Chan, C. Xiao, Y. Dai, M. Xie, and J. Hao, Nat. Commun. **10**, 1775 (2019).
[24]B. Huang, G. Clark, D. R. Klein, D. MacNeill, E. Navarro-Moratalla, K. L. Seyler, N. Wilson, M. A. McGuire, D. H. Cobden, D. Xiao, W. Yao, P. Jarillo-Herrero, and X. Xu, Nat. Nanotechnol. **13**, 544 (2018).
[25]Y. Liu, N. O. Weiss, X. Duan, H. C. Cheng, Y. Huang, and X. Duan, Nat. Rev. Mater. **1**, 16042 (2016).
[26]D. Jariwala, T. J. Marks, and M. C. Hersam, Nat. Mater. **16**, 170 (2017).
[27]H. Zhao, X. Chen, G. Wang, Y. Qiu, and L. Guo, 2D Mater. **6**, 032002 (2019).
[28]H. Hosono, J. Non. Cryst. Solids **352**, 851 (2006).
[29]M. Sistiaga and A. R. Pierna, J. Non. Cryst. Solids **329**, 184 (2003).
[30]D. Adler and E. J. Yoffa, Phys. Rev. Lett. **36**, 1197 (1976).
[31]J. Y. Kwon, D. J. Lee, and K. B. Kim, Electron. Mater. Lett. **7**, 1 (2011).
[32]J. Nai, H. Yin, T. You, L. Zheng, J. Zhang, P. Wang, Z. Jin, Y. Tian, J. Liu, Z. Tang, and L. Guo, Adv. Energy Mater. **5**, 1401880 (2015).
[33]R. D. L. Smith, M. S. Prévot, R. D. Fagan, Z. Zhang, P. A. Sedach, M. K. J. Siu, S. Trudel, and C. P. Berlinguette, Science **340**, 60 (2013).
[34]A. I. Kingon, J. P. Maria, and S. K. Streiffer, Nature **406**, 1032 (2000).
[35]L. Manchanda, M. D. Morris, M. L. Green, R. B. Van Dover, F. Klemens, T. W. Sorsch, P. J. Silverman, G. Wilk, B. Busch, and S. Aravamudhan, Microelectron. Eng. **59**, 351 (2001).
[36]C.-T. Toh, H. Zhang, J. Lin, A. S. Mayorov, Y.-P. Wang, C. M. Orofeo, D. B. Ferry, H. Andersen, N. Kakenov, Z. Guo, I. H. Abidi, H. Sims, K. Suenaga, S. T. Pantelides, and B. Özyilmaz, Nature **577**, 199 (2020).
[37]Z. Huang, T. Zhang, J. Liu, L. Zhang, Y. Jin, J. Wang, K. Jiang, S. Fan, and Q. Li, ACS Appl. Electron. Mater. **1**, 1314 (2019).
[38]Z. Yang, J. Hao, S. Yuan, S. Lin, H. M. Yau, J. Dai, and S. P. Lau, Adv. Mater. **27**, 3748 (2015).
[39]K. K. Chattopadhyay, D. Banerjee, N. S. Das, and D. Sarkar, Carbon **72**, 4 (2014).
[40]S. Yano, K. Sato, J. Suzuki, H. Imai, and Y. Oaki, Commun. Chem. **2**, 97 (2019).
[41]W. J. Joo, J. H. Lee, Y. Jang, S. G. Kang, Y. N. Kwon, J. Chung, S. Lee, C. Kim, T. H. Kim, C. W. Yang, U. J. Kim, B. L. Choi, D. Whang, and S. W. Hwang, Sci. Adv. **3**, e1601821 (2017).
[42]M. M. Bhunia, K. Panigrahi, S. Das, K. K. Chattopadhyay, and P. Chattopadhyay, Carbon **139**, 1010 (2018).
[43]L. Wu, A. Longo, N. Y. Dzade, A. Sharma, M. M. R. M. Hendrix, A. A. Bol, N. H. de Leeuw, E. J. M. Hensen, and J. P. Hofmann, ChemSusChem **12**, 4383 (2019).
[44]W. Fu, S. Yang, H. Yang, B. Guo, and Z. Huang, J. Mater. Chem. A **7**, 18799 (2019).
[45]M. Durandurdu, J. Non. Cryst. Solids **427**, 41 (2015).
[46]N. R. Glavin, C. Muratore, M. L. Jespersen, J. Hu, P. T. Hagerty, A. M. Hilton, A. T. Blake, C. A. Grabowski, M. F. Durstock, M. E. McConney, D. M. Hilgefort, T. S. Fisher, and A. A. Voevodin, Adv. Funct. Mater. **26**, 2640 (2016).
[47]B. Verberck, Nat. Phys. **13**, 205 (2017).
[48]J. Kotakoski, A. V. Krasheninnikov, U. Kaiser, and J. C. Meyer, Phys. Rev. Lett. **106**, 105505 (2011).
[49]J. W. Suk, A. Kitt, C. W. Magnuson, Y. Hao, S. Ahmed, J. An, A. K. Swan, B. B. Goldberg, and R. S. Ruoff, ACS Nano **5**, 6916 (2011).
[50]G. Bai, S. Yuan, Y. Zhao, Z. Yang, S. Y. Choi, Y. Chai, S. F. Yu, S. P. Lau, and J. Hao, Adv. Mater. **28**, 7472 (2016).
[51]Z. Yang, Z. Wu, Y. Lyu, and J. Hao, InfoMat **1**, 98 (2019).
[52]M. Hafeez, L. Gan, H. Li, Y. Ma, and T. Zhai, Adv. Mater. **28**, 8296 (2016).
[53]Y. Zhang, Y. Yao, M. G. Sendeku, L. Yin, X. Zhan, F. Wang, Z. Wang, and J. He, Adv. Mater. **31**, 1901694 (2019).
[54]Y. Zhang, L. Zhang, and C. Zhou, Acc. Chem. Res. **46**, 2329 (2013).
[55]Z. Cai, B. Liu, X. Zou, and H.-M. Cheng, Chem. Rev. **118**, 6091 (2018).
[56]J. Chen, Y. Wen, Y. Guo, B. Wu, L. Huang, Y. Xue, D. Geng, D. Wang, G. Yu, and Y. Liu, J. Am. Chem. Soc. **133**, 17548 (2011).
[57]M. H. Rümmeli, A. Bachmatiuk, A. Scott, F. Börrnert, J. H. Warner, V. Hoffman, J. H. Lin, G. Cuniberti, and B. Büchner, ACS Nano **4**, 4206 (2010).
[58]J. Zhao, G. Zhu, W. W. Huang, Z. He, X. Feng, Y. Ma, X. Dong, Q. Fan, L. Wang, Z. Hu, Y. Lü, and W. W. Huang, J. Mater. Chem. **22**, 19679 (2012).
[59]Q. H. Wang, Z. Jin, K. K. Kim, A. J. Hilmer, G. L. C. Paulus, C. J. Shih, M. H. Ham, J. D. Sanchez-Yamagishi, K. Watanabe, T. Taniguchi, J. Kong, P. Jarillo-Herrero, and M. S. Strano, Nat. Chem. **4**, 724 (2012).
[60]J. D. Wood, S. W. Schmucker, A. S. Lyons, E. Pop, and J. W. Lyding, Nano Lett. **11**, 4547 (2011).
[61]X. A. Li, Z. R. Liu, B. L. Wang, J. P. Yang, Y. W. Ma, X. M. Feng, W. Huang, and M. F. Gu, Synth. Met. **174**, 50 (2013).
[62]W. Huang, J. Y. Dai, and J. H. Hao, Appl. Phys. Lett. **97**, 162905 (2010).
[63]C. Ahn, J. Lee, H.-U. Kim, H. Bark, M. Jeon, G. H. Ryu, Z. Lee, G. Y. Yeom, K. Kim, J. Jung, Y. Kim, C. Lee, and T. Kim, Adv. Mater. **27**, 5223 (2015).
[64]M. Li, D. Liu, D. Wei, X. Song, D. Wei, and A. T. S. Wee, Adv. Sci. **3**, 1600003 (2016).
[65]Y. N. Li, R. Z. Wang, C. H. Su, Z. Shen, Y. F. Zhang, and H. Yan, J. Alloys Compd. **705**, 734 (2017).
[66]H. G. Kim and H. B. R. Lee, Chem. Mater. **29**, 3809 (2017).
[67]S. Shin, Z. Jin, D. H. Kwon, R. Bose, and Y.-S. Min, Langmuir **31**, 1196 (2015).
[68]M. Song, H. Tan, X. Li, A. I. Y. Tok, P. Liang, D. Chao, and H. J. Fan, "Atomic-layer-deposited amorphous $MoS_2$ for durable and flexible Li–$O_2$ batteries," Small Methods (published online, 2019).
[69]A. J. Mannix, B. Kiraly, M. C. Hersam, and N. P. Guisinger, Nat. Rev. Chem. **1**, 0014 (2017).
[70]Z. Yang and J. Hao, J. Mater. Chem. C **4**, 8859 (2016).
[71]J. Zhou, Q. Zeng, D. Lv, L. Sun, L. Niu, W. Fu, F. Liu, Z. Shen, C. Jin, and Z. Liu, Nano Lett. **15**, 6400 (2015).
[72]Y. Zhang and J. Hao, J. Appl. Phys. **113**, 184112 (2013).
[73]G. Bai, Y. Zhang, and J. Hao, Sci. Rep. **4**, 5724 (2014).
[74]J. Hao, Y. Zhang, and X. Wei, Angew. Chem. Int. Ed. **50**, 6876 (2011).
[75]O. Nakagawara, T. Shimuta, T. Makino, S. Arai, H. Tabata, and T. Kawai, Appl. Phys. Lett. **77**, 3257 (2000).
[76]H. Tabata, H. Tanaka, and T. Kawai, Appl. Phys. Lett. **65**, 1970 (1994).
[77]Z. Yang, W. Huang, and J. Hao, Appl. Phys. Lett. **103**, 031919 (2013).

[78]Y. Zhang, G. Gao, H. L. W. Chan, J. Dai, Y. Wang, and J. Hao, Adv. Mater. **24**, 1729 (2012).
[79]Z. Yang and J. Hao, J. Appl. Phys. **112**, 054110 (2012).
[80]W. Jie, Z. Yang, F. Zhang, G. Bai, C. W. Leung, and J. Hao, ACS Nano **11**, 6950 (2017).
[81]G. Bai, Z. Yang, H. Lin, W. Jie, and J. Hao, Nanoscale **10**, 9261 (2018).
[82]A. F. Rigosi, H. M. Hill, N. R. Glavin, S. J. Pookpanratana, Y. Yang, A. G. Boosalis, J. Hu, A. Rice, A. A. Allerman, N. V. Nguyen, C. A. Hacker, R. E. Elmquist, A. R. Hight Walker, and D. B. Newell, 2D Mater. **5**, 011011 (2018).
[83]A. F. Rigosi, C.-I. Liu, N. R. Glavin, Y. Yang, H. M. Hill, J. Hu, A. R. Hight Walker, C. A. Richter, R. E. Elmquist, and D. B. Newell, ACS Omega **2**, 2326 (2017).
[84]K. H. Lee, H.-J. Shin, J. Lee, I. Lee, G.-H. Kim, J.-Y. Choi, and S.-W. Kim, Nano Lett. **12**, 714 (2012).
[85]H. Liu, Y. Du, Y. Deng, and P. D. Ye, Chem. Soc. Rev. **44**, 2732 (2015).
[86]J. Qiao, X. Kong, Z. X. Hu, F. Yang, and W. Ji, Nat. Commun. **5**, 4475 (2014).
[87]J. O. Island, G. A. Steele, H. S. J. Van Der Zant, and A. Castellanos-Gomez, 2D Mater. **2**, 011002 (2015).
[88]A. Favron, E. Gaufrès, F. Fossard, A. L. Phaneuf-Laheureux, N. Y. W. Tang, P. L. Lévesque, A. Loiseau, R. Leonelli, S. Francoeur, and R. Martel, Nat. Mater. **14**, 826 (2015).
[89]M. I. Serna, S. H. Yoo, S. Moreno, Y. Xi, J. P. Oviedo, H. Choi, H. N. Alshareef, M. J. Kim, M. Minary-Jolandan, and M. A. Quevedo-Lopez, ACS Nano **10**, 6054 (2016).
[90]X. Zhang, Y. Zhang, B. Bin Yu, X. L. Yin, W. J. Jiang, Y. Jiang, J. S. Hu, and L. J. Wan, J. Mater. Chem. A **3**, 19277 (2015).
[91]Q. Abbas, H. Liang, J. Shi, Y. Chen, X. Xia, A. Ul Ahmad, J. Liu, and G. Du, Mater. Lett. **227**, 284 (2018).
[92]R. Wang, P. Sun, H. Wang, and X. Wang, Electrochim. Acta **258**, 876 (2017).
[93]Y. Tian, X. Zhao, L. Shen, F. Meng, L. Tang, Y. Deng, and Z. Wang, Mater. Lett. **60**, 527 (2006).
[94]Y. Peng, Z. Meng, C. Zhong, J. Lu, Z. Yang, and Y. Qian, Mater. Chem. Phys. **73**, 327 (2002).
[95]J. Y. Huang, H. Yasuda, and H. Mori, J. Am. Ceram. Soc. **83**, 403 (2000).
[96]J. Wang, Y. Qiao, T. Wang, H. Yu, Y. Feng, and L. Li, Inorg. Chem. Commun. **92**, 110 (2018).
[97]M. Moshe, I. Levin, H. Aharoni, R. Kupferman, and E. Sharon, Proc. Natl. Acad. Sci. U. S. A. **112**, 10873 (2015).
[98]M. Cargnello, J. J. Delgado Jaén, J. C. Hernández Garrido, K. Bakhmutsky, T. Montini, J. J. Calvino Gámez, R. J. Gorte, and P. Fornasiero, Science **337**, 713 (2012).
[99]D.-H. Lee, Y.-J. Chang, G. S. Herman, and C.-H. Chang, Adv. Mater. **19**, 843 (2007).
[100]E. Uchaker, Y. Z. Zheng, S. Li, S. L. Candelaria, S. Hu, and G. Z. Cao, J. Mater. Chem. A **2**, 18208 (2014).
[101]P. Avouris, Nano Lett. **10**, 4285 (2010).
[102]Y. Zhu, S. Murali, W. Cai, X. Li, J. W. Suk, J. R. Potts, and R. S. Ruoff, Adv. Mater. **22**, 3906 (2010).
[103]B. Wu, H. M. Tuncer, A. Katsounaros, W. Wu, M. T. Cole, K. Ying, L. Zhang, W. I. Milne, and Y. Hao, Carbon **77**, 814 (2014).
[104]M. Chiesa and S. K. Das, Colloids Surf. A **335**, 88 (2009).
[105]A. Kumar, M. Wilson, and M. F. Thorpe, J. Phys. Condens. Matter **24**, 485003 (2012).
[106]Z.-S. Wu, S. Pei, W. Ren, D. Tang, L. Gao, B. Liu, F. Li, C. Liu, and H.-M. Cheng, Adv. Mater. **21**, 1756 (2009).
[107]S. Goswami, U. N. Maiti, S. Maiti, S. Nandy, M. K. Mitra, and K. K. Chattopadhyay, Carbon **49**, 2245 (2011).
[108]H. Li, J. Wu, Z. Yin, and H. Zhang, Acc. Chem. Res. **47**, 1067 (2014).
[109]S. Yuan, S.-Y. Pang, and J. Hao, Appl. Phys. Rev. **7**, 021304 (2020).
[110]C. G. Morales-Guio and X. Hu, Acc. Chem. Res. **47**, 2671 (2014).
[111]P. Cao, J. Peng, J. Li, and M. Zhai, J. Power Sources **347**, 210 (2017).
[112]J. Deng, H. Li, J. Xiao, Y. Tu, D. Deng, H. Yang, H. Tian, J. Li, P. Ren, and X. Bao, Energy Environ. Sci. **8**, 1594 (2015).
[113]G. R. Bhimanapati, T. Hankins, Y. Lei, R. A. Vilá, I. Fuller, M. Terrones, and J. A. Robinson, ACS Appl. Mater. Interfaces **8**, 22190 (2016).
[114]Q. Ding, B. Song, P. Xu, and S. Jin, Chem **1**, 699 (2016).
[115]B. W. Ahn, T. Y. Kim, S. H. Kim, Y. Il Song, and S. J. Suh, Appl. Surf. Sci. **432**, 183 (2018).
[116]C. G. Morales-Guio, S. D. Tilley, H. Vrubel, M. Graïzel, and X. Hu, Nat. Commun. **5**, 3059 (2014).
[117]K. Zhu, X. Wang, J. Liu, S. Li, H. Wang, L. Yang, S. Liu, and T. Xie, ACS Sustainable Chem. Eng. **5**, 8025 (2017).
[118]Y. Zhang, W. Sun, X. Rui, B. Li, H. T. Tan, G. Guo, S. Madhavi, Y. Zong, and Q. Yan, Small **11**, 3694 (2015).
[119]M. L. Zou, J. D. Chen, L. F. Xiao, H. Zhu, T. T. Yang, M. Zhang, and M. L. Du, J. Mater. Chem. A **3**, 18090 (2015).
[120]S.-Y. Pang, Y.-T. Wong, S. Yuan, Y. Liu, M.-K. Tsang, Z. Yang, H. Huang, W.-T. Wong, and J. Hao, J. Am. Chem. Soc. **141**, 9610 (2019).
[121]D. Merki, S. Fierro, H. Vrubel, and X. Hu, Chem. Sci. **2**, 1262 (2011).
[122]J. Lu, L. Li, J.-B. Park, Y.-K. Sun, F. Wu, and K. Amine, Chem. Rev. **114**, 5611 (2014).
[123]J. Hou, B. Zhang, Z. Li, S. Cao, Y. Sun, Y. Wu, Z. Gao, and L. Sun, ACS Catal. **8**, 4612 (2018).
[124]Y. Wang, Z. Shi, Y. Huang, Y. Ma, C. Wang, M. Chen, and Y. Chen, J. Phys. Chem. C **113**, 13103 (2009).
[125]C. Hu, X. Wang, P. Miao, L. Zhang, B. Song, W. Liu, Z. Lv, Y. Zhang, Y. Sui, J. Tang, Y. Yang, B. Song, and P. Xu, ACS Appl. Mater. Interfaces **9**, 18362 (2017).
[126]X. Wang, P. Wang, J. Wang, W. Hu, X. Zhou, N. Guo, H. Huang, S. Sun, H. Shen, T. Lin, M. Tang, L. Liao, A. Jiang, J. Sun, X. Meng, X. Chen, W. Lu, and J. Chu, Adv. Mater. **27**, 6575 (2015).
[127]D. Kufer and G. Konstantatos, Nano Lett. **15**, 7307 (2015).
[128]W. Yang, G. Chen, Z. Shi, C. C. Liu, L. Zhang, G. Xie, M. Cheng, D. Wang, R. Yang, D. Shi, K. Watanabe, T. Taniguchi, Y. Yao, Y. Zhang, and G. Zhang, Nat. Mater. **12**, 792 (2013).
[129]C. R. Dean, A. F. Young, I. Meric, C. Lee, L. Wang, S. Sorgenfrei, K. Watanabe, T. Taniguchi, P. Kim, K. L. Shepard, and J. Hone, Nat. Nanotechnol. **5**, 722 (2010).
[130]R. Zedlitz, M. Heintze, and M. B. Schubert, J. Non. Cryst. Solids **198**, 403 (1996).
[131]C. Steinborn, M. Herrmann, U. Keitel, A. Schönecker, J. Räthel, D. Rafaja, and J. Eichler, J. Eur. Ceram. Soc. **33**, 1225 (2013).
[132]K. K. Kim, A. Hsu, X. Jia, S. M. Kim, Y. Shi, M. Dresselhaus, T. Palacios, and J. Kong, ACS Nano **6**, 8583 (2012).
[133]S. Ang and S. Wilson, J. Electrochem. Soc. **134**, 1254 (1987).
[134]Y. Yang, H. Du, Q. Xue, X. Wei, Z. Yang, C. Xu, D. Lin, W. Jie, and J. Hao, Nano Energy **57**, 566 (2019).
[135]H. Du, J. Chen, M. Tu, S. Luo, S. Li, S. Yuan, T. Gong, W. Huang, W. Jie, and J. Hao, J. Mater. Chem. C **7**, 12160 (2019).
[136]Y.-R. Jeon, Y. Abbas, A. S. Sokolov, S. Kim, B. Ku, and C. Choi, ACS Appl. Mater. Interfaces **11**, 23329 (2019).
[137]T. Yamada, T. Masuzawa, T. Ebisudani, K. Okano, and T. Taniguchi, Appl. Phys. Lett. **104**, 221603 (2014).
[138]B. Sirota, N. Glavin, S. Krylyuk, A. V. Davydov, and A. A. Voevodin, Sci. Rep. **8**, 8668 (2018).
[139]M. Huang, M. Wang, C. Chen, Z. Ma, X. Li, J. Han, and Y. Wu, Adv. Mater. **28**, 3481 (2016).
[140]Q. Guo, A. Pospischil, M. Bhuiyan, H. Jiang, H. Tian, D. Farmer, B. Deng, C. Li, S. J. Han, H. Wang, Q. Xia, T. P. Ma, T. Mueller, and F. Xia, Nano Lett. **16**, 4648 (2016).
[141]V. Tran, R. Soklaski, Y. Liang, and L. Yang, Phys. Rev. B **89**, 235319 (2014).
[142]F. Xia, H. Wang, and Y. Jia, Nat. Commun. **5**, 4458 (2014).
[143]M. Z. Bellus, Z. Yang, J. Hao, S. P. Lau, and H. Zhao, 2D Mater. **4**, 025063 (2017).
[144]M. Z. Bellus, Z. Yang, P. Zereshki, J. Hao, S. P. Lau, and H. Zhao, Nanoscale Horiz. **4**, 236 (2019).